Interactions of the heliospheric current and plasma sheets with the bow shock: Cluster and Polar observations in the magnetosheath

Nelson C. Maynard,[1] Charles J. Farrugia,[1] William J. Burke,[2] Daniel M. Ober,[2] Jack D. Scudder,[3] Forrest S. Mozer,[4] Christopher T. Russell,[5] Henri Rème,[6] Christopher Mouikis,[1] and Keith D. Siebert[7]

[1] On 12 March 2001, the Polar and Cluster spacecraft were at subsolar and cusp latitudes in the dayside magnetosheath, respectively, where they monitored the passage by Earth of a large-scale planar structure containing the high-density heliospheric plasma sheet (HPS) and the embedded current sheet. Over significant intervals, as the magnetic hole of the HPS passed Cluster and Polar, magnetic field strengths |**B**| were much smaller than expected for the shocked interplanetary magnetic field. For short periods, |**B**| even fell below values measured by ACE in the upstream solar wind. Within the magnetic hole the ratio of plasma thermal and magnetic pressures (plasma β) was consistently >100 and exceeded 1000. A temporary increase in lag times for identifiable features in **B** components to propagate from the location of ACE to those of Cluster and Polar was associated with the expansion (and subsequent compression) of the magnetic field and observed low |**B**|. Triangulation of the propagation velocity of these features across the four Cluster spacecraft configuration showed consistency with the measured component of ion velocity normal to the large-scale planar structure. **B** experienced large-amplitude wave activity, including fast magnetosonic waves. Within the low |**B**| region, guiding center behavior was disrupted and ions were subject to hydrodynamic rather than magnetohydrodynamic forcing. Under the reported conditions, a significant portion of the interplanetary coupling to the magnetosphere should proceed through interaction with the low-latitude boundary layer. Data acquired during a nearly simultaneous high-latitude pass of a Defense Meteorological Satellites Program satellite are consistent with this conjecture.

1. Introduction

[2] Understanding the time scales and mechanisms through which the solar wind and interplanetary magnetic field (IMF) couple to the magnetosphere provides a basis for physics-based space weather predictions. The interactions of the heliospheric current sheet (HCS), and associated heliospheric plasma sheet (HPS), with the Earth's bow shock, magnetosheath, and magnetosphere are subjects that have been given scant attention. Yet because of their relations to the "sector structures" in the solar wind, these crossings are occurrences that must happen at least twice per solar rotation. The aim of this paper is to examine one such set of interactions that occurred on 12 March 2001. We show that the extremely high plasma density and low magnetic field result in a mixture of hydrodynamic and magnetohydrodynamic (MHD) forcing in the coupling between the solar wind and the IMF to the magnetosphere. By hydrodynamic forcing we mean that the diversion of ions around the magnetosphere is dominated by inertia and pressure gradients from the stagnation of flow at the nose. Its coupling to the magnetosphere is through closed magnetic field lines of the low-latitude boundary layer (LLBL) [*Sonnerup*, 1980; *Lotko et al.*, 1987]. By MHD forcing we mean that in response to the stagnation pressure gradient the ions are

[1]Space Science Center, University of New Hampshire, Durham, New Hampshire, USA.
[2]Air Force Research Laboratory, Hanscom Air Force Base, Bedford, Massachusetts, USA.
[3]Department of Physics and Astronomy, University of Iowa, Iowa City, Iowa, USA.
[4]Space Sciences Laboratory, University of California, Berkeley, California, USA.
[5]Institute of Geophysics and Planetary Physics, University of California, Los Angeles, California, USA.
[6]Centre d'Etude Spatiale des Rayonnements, CNRS, Toulouse, France.
[7]Applied Research Associates, Inc., Nashua, New Hampshire, USA.

constrained to move either parallel to the magnetic field or with guiding center motion perpendicular to the magnetic field until reaching the magnetopause. Coupling to the magnetosphere is primarily through magnetic merging, creating open magnetic field lines in the high-latitude boundary layer (HLBL) [*Dungey*, 1961]. By ion demagnetization, we mean that the ions no longer conform to guiding center motion [*Northrup*, 1964]. As a result, the ion pressure tensor does not remain cylindrically symmetric about the magnetic field strength **B**, the $\mathbf{E} \times \mathbf{B}/B^2$ is not equal to $V_{\perp i}$, and the MHD approximation is no longer valid. This is the third in a series addressing how directional discontinuities and associated pressure changes in the solar wind interact with the bow shock, magnetosheath, and magnetosphere [*Maynard et al.*, 2007, 2008].

[3] Between 1200 and 1300 UT on 12 March 2001, the HCS and the associated HPS, with a scale size of $\sim 10^6$ km, interacted with the Earth's bow shock and dayside magnetosheath. The fortuitous locations of seven satellites (ACE, Wind, Polar, and the four-satellite Cluster constellation) allowed these features to be tracked from the solar wind into the magnetosheath. Within a magnetic hole (or a pronounced magnetic field depression) in the HPS, ACE and Wind measured a factor of 2 increase in density from 10 to 20 cm^{-3}. As the IMF decreased from 9 nT to between 3 and 5 nT, plasma β_i ($\beta_{e,i}$ is the ratio of the thermal and magnetic pressures; i.e., $nk_B T_{e,i}/B^2/\mu_0$) ranged up to 10 at ACE. Magnetosheath responses were remarkable; densities reached 130 cm^{-3}, |**B**| occasionally fell below relatable IMF values, and β_i exceeded 1000. This event study explores possible causes of these variations.

[4] The discovery of sector structures in the IMF [*Ness and Wilcox*, 1964; *Wilcox and Ness*, 1965] led to the identification of the HCS as a continuous wavy structure that divides interplanetary space around the Sun into two hemispheres characterized by opposite magnetic polarities [e.g., *Schulz*, 1973; *Smith et al.*, 1978]. The thin HCS is associated with a high-density, low-velocity solar wind and a reversal of IMF polarity [e.g., *Kivelson and Russell*, 1995]. The geometry of the boundary between the toward and away polarities of the IMF need not be at a fixed heliocentric latitude. Because of coronal activity, the HCS may have a wavy structure, which has been compared to the shape of a ballerina's skirt (see *Hundhausen* [1977, Figure 15], based on earlier work by *Pneuman and Kopp* [1971]). While B_X and B_Y are tied to this sector structure in an average sense, B_Z variations are more random and less predictable. *Winterhalter et al.* [1994] found that the HCS is often embedded in a significantly thicker region of enhanced plasma density and depressed magnetic field. They defined the extent of the HPS as coextensive with the high-β region. The location of the broad distinct peak in β within the HPS does not often coincide with that of the HCS. The HPS has a median thickness of $\sim 320{,}000$ km compared with a nominal HCS thickness of 1900 km.

[5] In an early study, *Klein and Burlaga* [1980] defined the sector boundary crossing current sheet as the total region between areas of stability on both sides of the transition. Minimum variance analysis established that this macroscale HCS has a large planar structure. Multiple directional discontinuities and associated current sheets are often observed within sector boundary crossings. Each can be regarded as crossings of the HCS, thus allowing conjectures that the HCS contains wave-like structures. *Winterhalter et al.* [1994] used this narrower HCS definition while considering its relationship to the HPS. *Crooker et al.* [1993, 1996] suggested an alternative definition to the wave-like structure interpretation. They attribute multiple discontinuities encountered within sector crossings to different current sheets reflecting time-dependent sources in the coronal streamer belt. In some cases they could even wind up as intertwined flux ropes. *Kahler and Lin* [1994] argued that electron heat fluxes on both sides of a discontinuity should be away from the Sun if the structure event represents a direct crossing of the HCS. Heat fluxes toward the Sun would then be regarded as signatures of kinks or wave structures in the HCS. *Crooker et al.* [1996] used the heat flux argument to conclude that the most intense HPS events were associated with true magnetic polarity reversals. Through compressions, even intertwined flux tubes become parts of the expected large-scale planar structure.

[6] Ordinarily, interactions of the Earth's bow shock with solar wind features increase downstream densities by a factor of ~ 3.8. Further compression occurs as the shocked plasma approaches the magnetopause. The magnetic field magnitude increases by the same factor when its direction is perpendicular to the shock normal. The scaling factor reduces to 1 when the field direction is parallel to the shock normal. Hence observing magnetic field magnitudes downstream of a quasi-perpendicular shock that are below their solar wind counterparts needs to be explained.

[7] The IMF B_X influences the timing of solar wind features interacting with the magnetosphere. *Maynard et al.* [2001b] reported small-scale solar wind–IMF features whose variations correlated with those of dayside ionospheric electric fields and 557.7 nm emissions. However, the observed lag times were significantly less than the advection delay between L_1 and the magnetopause. They attributed this to tilted phase fronts containing interplanetary **E** and **B** in the solar wind. The polarity of IMF B_X controls which magnetospheric hemisphere is first to interact with structures in the solar wind, often sooner than predicted by advection times. *Weimer et al.* [2002], using four satellites in the solar wind, verified this concept and showed that the phase plane can shift its orientation dramatically on scales of tens of minutes, depending on the IMF orientation and the presence (or absence) of B_X. *Maynard et al.* [2006] showed that to change the tilts of phase fronts, magnetic flux must compress in some regions and expand in others. They correlated a 557.7 nm auroral intensification in the dayside cusp to a compression monitored by Cluster. Satellites at off-equatorial locations in the magnetosheath should encounter similar timing differences and magnetic flux compressions/rarefactions.

[8] Interactions that occur between the solar wind and magnetosphere system as the IMF approaches zero approximate in one sense a "ground state" of the magnetosphere system. Magnetic merging between the IMF and the Earth's field completely turns off and coupling across the magnetopause is driven via diffusive processes, such as viscosity, resistivity, or flow shears associated with the Kelvin-Helmholtz instability. *Sonnerup et al.* [2001] used the Inte-
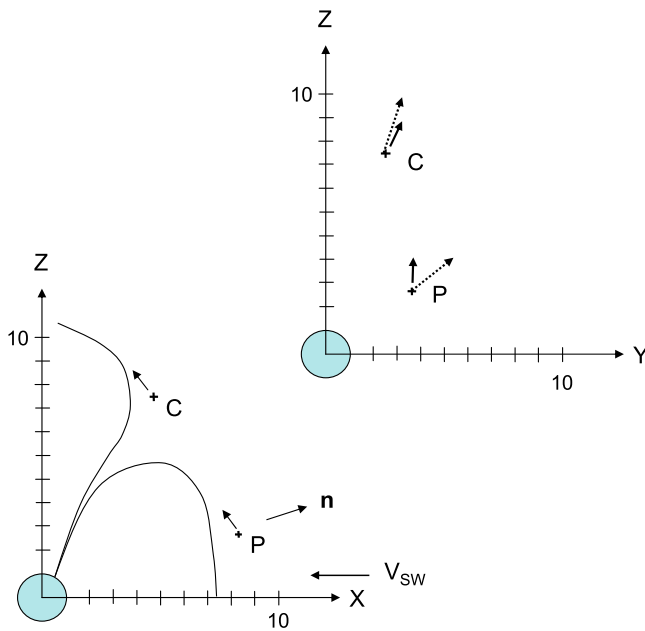
Figure 1. Schematic representation of locations of Polar (P) and the Cluster constellation (C) in the GSE *X-Z* and *Y-Z* planes. The dotted vectors in the *Y-Z* plane represent the direction of flow if it is purely away from the stagnation region at the nose of the magnetopause. The solid vectors at each location represent typical background ion velocities measured by Cluster 1 and Polar. The vector **n** is the normal to the incoming planar structure determined from minimum variance analysis of **B**. A crude representation of the magnetopause is also shown.

grated Space-weather prediction Model (ISM), a global MHD simulation code [*White et al.*, 2001], to explore ground state properties including quantitative analysis of low-latitude boundary layer coupling to the ionosphere. They demonstrated that tailward flowing LLBL plasmas extend along the flanks of the magnetosphere with an interior, sunward return channel. With a solar wind velocity of 400 km s^{-1}, a density of 5 cm^{-3}, and an ionospheric Pedersen conductance of 6 mho, the simulated cross-polar-cap potential was 30 kV.

[9] After describing data sources and simulation techniques used in this study, we present solar wind plasma and magnetic field measurements from ACE and Wind to establish the properties of the HPS and HCS crossings. Responses to HPS and HCS passage in the magnetosheath as observed by Polar and Cluster are then considered. The discussion explores possible causes and consequences of the very high β values and low magnetic fields in the magnetosheath, especially their effects on ion dynamics and the temporary dominance of hydrodynamic over MHD interactions with the magnetosphere.

2. Data Sources

[10] On 12 March 2001, the ACE and Wind spacecraft provided measurements of the solar wind and IMF at GSE locations of (227, −38, −5) R_E and (−37, −162, −30) R_E,

respectively. On ACE the Solar Wind Electron, Proton, and Alpha Monitor (SWEPAM) measured the solar wind velocity and density [*McComas et al.*, 1998] while a triaxial fluxgate magnetometer measured the three components (*X*, *Y*, and *Z*) of the IMF vector [*Smith et al.*, 1998]. Wind-measured ion densities and velocities with the Three-Dimensional Plasma and Energetic Particle Investigation (3DPL) instrument [*Lin et al.*, 1995] and IMF with fluxgate magnetometers of the Magnetic Field Investigation (MFI) [*Lepping et al.*, 1995]. Presented electron heat fluxes and proton temperature anisotropies come from the Solar Wind Experiment (SWE) on Wind [*Ogilvie et al.*, 1995]. From the data sets of each satellite, β was calculated from the ion measurements.

[11] In March 2001 while Polar's apogee (9 R_E) was near the equatorial plane, its trajectory skimmed along the dayside magnetopause for long intervals, moving from south to north. From this vantage, Polar monitored magnetopause responses to temporal changes in the solar wind/IMF. On 12 March at 1230 UT it was located at GSE coordinates (8.36, 3.57, 2.56) R_E. This study uses data from three sensors on Polar. The Hydra Duo Deca Ion Electron Spectrometer (DDIES) consists of six pairs of electrostatic analyzers looking in different directions to acquire high-resolution energy and pitch angle spectra [*Scudder et al.*, 1995]. Distributions of electrons with energies between 1 eV and 10 keV and ions with energies per charge ratio of 10 eV q^{-1} to 10 keV q^{-1} are provided every 2.3 s. The electric field instrument (EFI) uses a biased double probe to measure vector electric fields from potential differences between three orthogonal pairs of spherical sensors [*Harvey et al.*, 1995]. Here we use data from the two antenna pairs in the satellite's spin plane. The Magnetic Field Experiment (MFE) consists of two orthogonal triaxial fluxgate magnetometers mounted on nonconducting booms [*Russell et al.*, 1995]. The digitization accuracy is ±0.09 nT, with a standard sampling rate of 9 Hz.

[12] The Cluster constellation was in a tetrahedral configuration with nominal interspacecraft separation distances of 600 km as it exited the magnetopause into the magnetosheath above the cusp at about 1210 UT. At 1230 UT Cluster 3 was located at GSE coordinates (4.43, 2.56, 8.37) R_E. Magnetosheath magnetic field measurements were made by triaxial fluxgate magnetometers on the four Cluster spacecraft [*Balogh et al.*, 2001]. The electric field and wave (EFW) instrument monitored electric field components in the ecliptic plane using two pairs of biased double probes [*Gustafsson et al.*, 1997]. The third component was calculated using the $\mathbf{E} \cdot \mathbf{B} = 0$ approximation. The Cluster Ion Spectrometer (CIS) experiment provided three-dimensional (3-D) ion distributions with mass per unit charge composition using the Composition and Distribution Function (CODIF) analyzer or 3-D ion distributions using the Hot Ion Analyzer (HIA) [*Rème et al.*, 2001]. Ion measurements are only available from Cluster 1, 3, and 4 during the period of interest. Figure 1 schematically indicates the relative locations of the Cluster constellation and of Polar.

[13] Defense Meteorological Satellites Program (DMSP) satellites are three-axis stabilized spacecraft that fly in circular, Sun synchronous, 98.7° inclined orbits at an altitude of ~840 km. DMSP F13's orbital plane was near the 1800–0600 local time meridian. Its scientific payload includes

sensors to monitor fluxes of auroral particles and the drift motions of ambient ions. The auroral particle sensors are mounted on the top surfaces of DMSP satellites to measure fluxes of downcoming electrons and ions in 19 logarithmically spaced energy steps between ~30 eV and 30 keV [*Hardy et al.*, 1984]. Full ion/electron spectra were compiled every second. Ion drift meters are located on the forward face of the DMSP spacecraft where they measure the horizontal (V_H) and vertical (V_V) components of cross-track plasma drifts. Although the drift meters measure V_H six times per second, data are presented here as 4 s averaged values [*Rich and Hairston*, 1984].

3. Simulation Techniques

[14] The ISM uses standard MHD equations augmented with hydrodynamic equations for the collisionally coupled neutral thermosphere [*White et al.*, 2001]. The code transitions seamlessly from pure MHD in the solar wind and magnetosphere to equations proper to the ionosphere and thermosphere at low altitudes. The ISM equations are solved within a 3-D computational domain extending upward from an interior spherical boundary at the bottom of the E layer (100 km) through the magnetosphere and into the solar wind. The spatial resolution of the ISM computational grid varies from a few hundred kilometers in the ionosphere to several R_E in the distant magnetotail downstream of the Earth. In the dayside magnetosphere and sunward to the boundary (40 R_E) the grid resolution was nearly uniform at 0.1 R_E, as necessary to resolve discontinuities in the solar wind and their interactions with the bow shock and magnetopause.

[15] In ISM computations, explicit viscosity was set equal to zero in the plasma momentum equation. An explicit resistivity term is included in Ohm's law only where the current density normal to **B** exceeds a specified threshold. In practice, this choice leads to an explicit, nonzero resistivity only near the subsolar magnetopause and in the nightside plasma sheet. Wherever dissipation is needed to maintain numerical stability, it arises via the partial donor-cell method (PDM) as formulated by *Hain* [1987]. The PDM adds diffusion in regions of steep gradients to prevent the generation of spurious extrema in the solution. This diffusion is manifest as resistivity. Dissipation is also necessary in the code to simulate nonlinear magnetic merging. It is important to note that the code solves for the configuration imposed by the boundary conditions by adding dissipation. Numerical experiments show that the merging rate is insensitive to the magnitude of numerical resistivity, leading to the conclusion that numerical resistivity enables the merging, but the merging rate is determined by the imposed boundary conditions. In the simulations described here, dayside dissipation was accomplished through the PDM in response to the imposed driving conditions rather than as a specific, current-dependent resistivity term.

4. Interplanetary Conditions

[16] Near midday on 12 March 2001 an HCS and associated HPS passed through near-Earth space. Figure 2 presents ACE and Wind data (black and red traces, respectively) for the 4 hour period that includes the HCS/HPS crossing. The traces in Figures 2a–2j show ion densities, velocities, tem-

peratures, dynamic pressure, magnitude and three GSE components of the magnetic field, β and the sum of the plasma and magnetic pressures plotted as functions of universal time at ACE. Despite the large separation between the spacecraft, these quantities tracked very well with data being measured by sensors on Wind acquired ~87 min after ACE. This lag was set to align their HCS encounters, centered on the blue line. Applying the definition in work by *Winterhalter et al.* [1994], we consider an HPS crossing as extending from the first rise in β_i to its final decrease to a constant level. These extents are marked in Figure 2i by two solid bars, black for ACE and red for Wind. Vertical lines serve to mark the HPS beginning and end points in plots. Note that the magnetic hole associated with the HPS encounter lasted longer at the location of ACE than that of Wind (Figure 2e). The HCS is offset from the center of the HPS and the region of highest β. *Winterhalter et al.* [1994] reported that in most cases both the HCS and the maximum β were offset from each other and from the center of the HPS.

[17] Figure 3 provides an expanded view of interplanetary data acquired during the hour of HPS and HCS encounters. Again solid bars in Figure 3i mark the duration of the HPS crossings. Note that reversals in **B** components occurred in stages across HCS. The first step included a reversal in B_Y and a change in the B_Z components. Four minutes later, in the second step or current layer, the polarities of B_X and B_Z reversed. At ACE a third step occurred in B_Z ~4 min later. We have highlighted these and other magnetic field component changes at ACE within the HPS interval. Seven vertical lines in Figure 3 mark significant changes in one or more magnetic field components: Line 1 highlights a reversal of B_Y; lines 2 and 3 mark key reversals of B_Z; line 4 marks reversals in both B_X and B_Z; and lines 5, 6, and 7 refer to changes in B_Y. As mentioned below, similar changes are found in the Polar and Cluster data streams. Within the magnetosheath they appeared in the same order but with temporal separations that differ from those observed in the solar wind. An additional dotted line in Figure 3, labeled 4+, marks the last B_Y reversal at ACE. Two changes seen at Cluster may relate to this change. As noted above, an 87 min delay between ACE and Wind aligns the signatures of the first current layer encounter.

[18] Electron heat flux directions relative to the local magnetic field can be used to determine whether satellite encounters with magnetic discontinuities were indeed HCS crossings. *Kahler and Lin* [1994] noted that the heat flux of electrons with energies >2 keV along **B** should always be directed away from the Sun. Thus heat flux polarity with respect to the local IMF **B** vector should reverse across the HCS. Indeed the direction of electron heat fluxes measured by the SWE experiment on Wind transitioned from antiparallel to parallel to **B** during the interval spanned by the red bar in Figure 3f, confirming our interpretation of the event as an HCS crossing (actual heat flux data are not shown). Electron heat flux measurements are not available from instrumentation on ACE.

[19] Figure 3j shows the angle θ between the **B** vector and the X_{GSE} axis. Note that θ was ~90° during the interval bounded by lines 2 and 4. Prior to 1113 UT, θ was ~75°; after 1122 UT it rapidly increased to ~135°. Larger angular differences occurred before θ settled near 120° for the
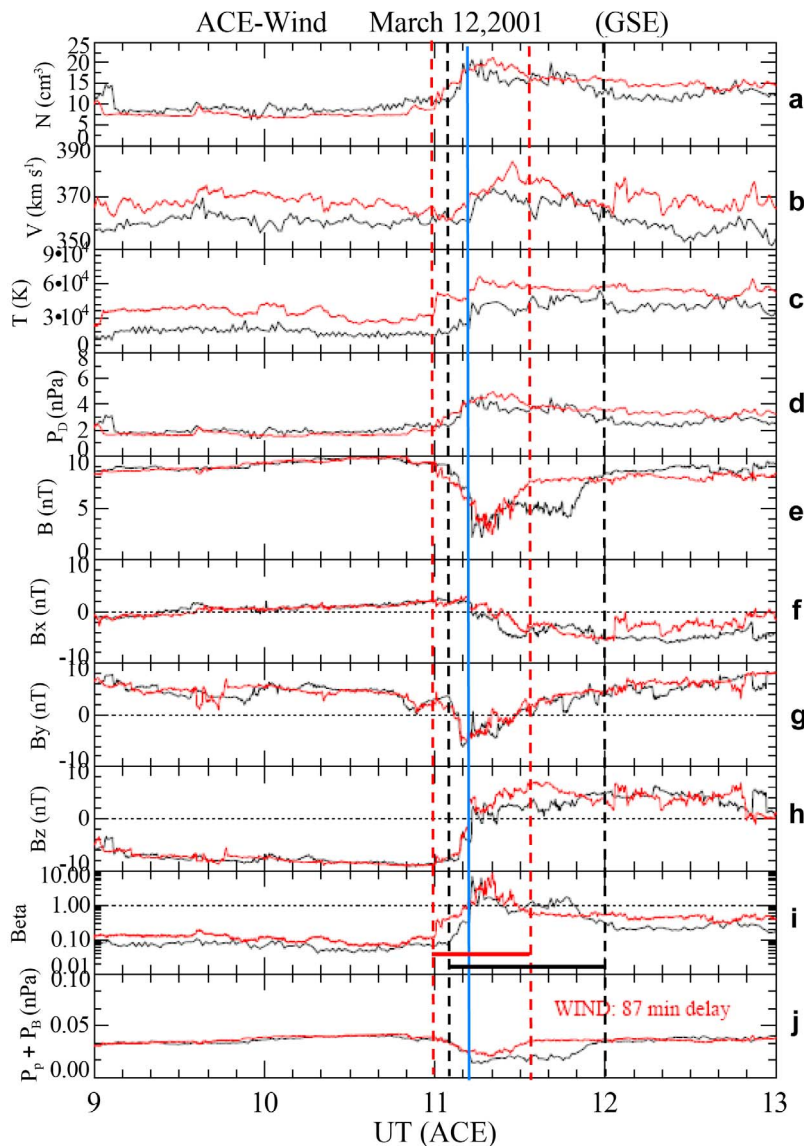
Figure 2. ACE (black) and Wind (red) data for the HCS crossing interval from 900 to 1300 UT on 12 March 2001; Wind data were lagged by 87 min. (a–d) Ion density (N), $|V|$, ion temperature (T), and dynamic pressure (P_D). (e–h) Magnitude and GSE components (X, Y, and Z) of B. (i) Ion β and (j) sum of the magnetic and ion thermal pressures. The dashed vertical lines and the solid bars in Figure 2i mark the boundaries of the HPS at ACE (black) and Wind (red).

remainder of the hour. Values of θ between 60° and 120° should produce quasi-perpendicular shocks in the subsolar region.

[20] To confirm that the observed HCS had a planar structure, we performed minimum variance analyses over two time intervals on data from each satellite and obtained similar results. Table 1 lists the normal vector directions, the ratios of middle to least eigenvalues, the value of B_N, and the standard deviations obtained in each analysis. The large ratio and close matches between normal vectors at the widely separated ACE and Wind satellites confirm that they did indeed cross a large-scale planar structure. The normal vectors obtained through analyses from the two 1 hour intervals subtend an angle of 21°. Note that B_N was

statistically zero at the location of Wind and 1.45 ± 0.94 nT at ACE.

5. Magnetosheath Responses at Polar and Cluster Locations

[21] After 1215 UT Polar was moving poleward just outside the magnetopause near 22° magnetic latitude (MLAT) and 13.2 magnetic local time (MLT). Cluster was in the magnetosheath at supracusp latitudes and slightly postnoon in MLT. Since the solar wind's dynamic pressure increased steadily from ~2.5 to 4 nPa (Figure 3d), the magnetopause was constrained to move earthward throughout the HCS encounter, allowing the outward moving Polar and Cluster satellites to remain in the magnetosheath.
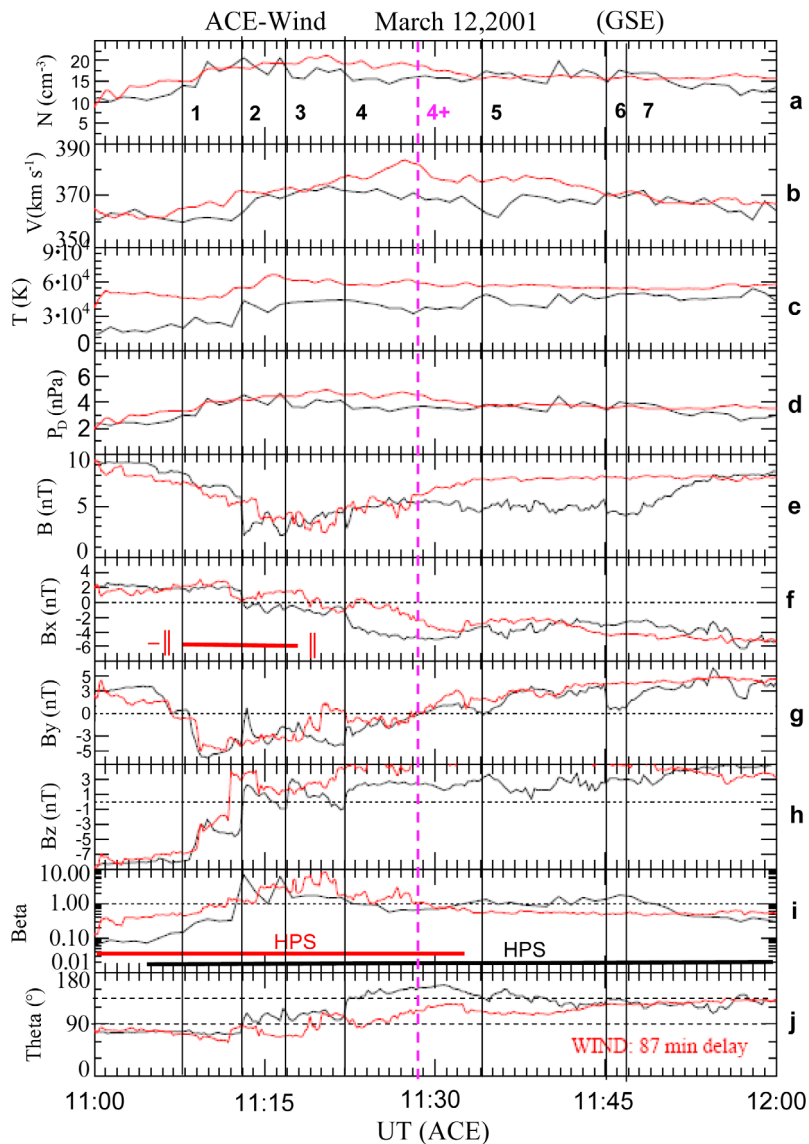
Figure 3. (a–i) the interval from 1100 to 1200 UT on 12 March 2001 in the same format as Figure 2. (j) Angle (θ) between the magnetic field and the X_{GSE} axis. The extents of the HPS at each spacecraft are shown by the solid bars in Figure 3i. The bar in Figure 3f shows the interval over which the electron heat flux measured by Wind reversed from antiparallel to parallel (see section 4). The vertical lines (labeled 1–9) mark features in ACE data that have corresponding variations in the Polar and Cluster measurements (see section 5, Figure 4, and Table 2). The purple line labeled 4+ also has a corresponding feature at Polar and Cluster, but it occurred out of sequence in the magnetosheath.

[22] Magnetic fields measured by Polar and Cluster 1 are plotted as functions of UT in Figure 4 in which vertical lines 1–7 mark changes in the components of B that correspond to those observed at the location of ACE. Table 2 lists the times of these polarity reversals at ACE, Polar, and Cluster. For reference, with a solar wind speed of 360 km s^{-1} the advection time from L$_1$ to 11 R_E, the approximate location of the subsolar bow shock, is 63.7 min. Attention is directed to the following three points of kinematic comparisons apparent in the listed time delays between various events in Table 2 and Figures 3 and 4.

[23] First, for magnetic field changes associated with lines 1 and 2, the observed 63 min lag between ACE and Polar,

Table 1. Minimum Variance Analyses

| Satellite	Interval (UT)	Normal Direction			Ratio	B_N (nT)	SD (nT)
		X	Y	Z			
ACE	1100–1300	0.8633	0.0186	0.5043	14.5	−1.46	± 0.72
ACE	1100–1200	0.8674	0.1344	0.4791	9.5	−1.45	± 0.94
Wind	1100–1400	0.8914	0.2937	0.3450	9.5	0.03	± 0.88
Wind	1215–1315	0.8650	0.4252	0.2661	29.0	0.06	± 0.52
Cluster 1	1215–1315	0.8751	0.1204	0.4688	9.2	−1.00	± 4.71
Cluster 3	1215–1315	0.8704	0.1120	0.4794	9.2	−1.20	± 4.62
Polar	1200–1300	0.9409	0.1934	0.2781	30.5	−0.19	± 2.48
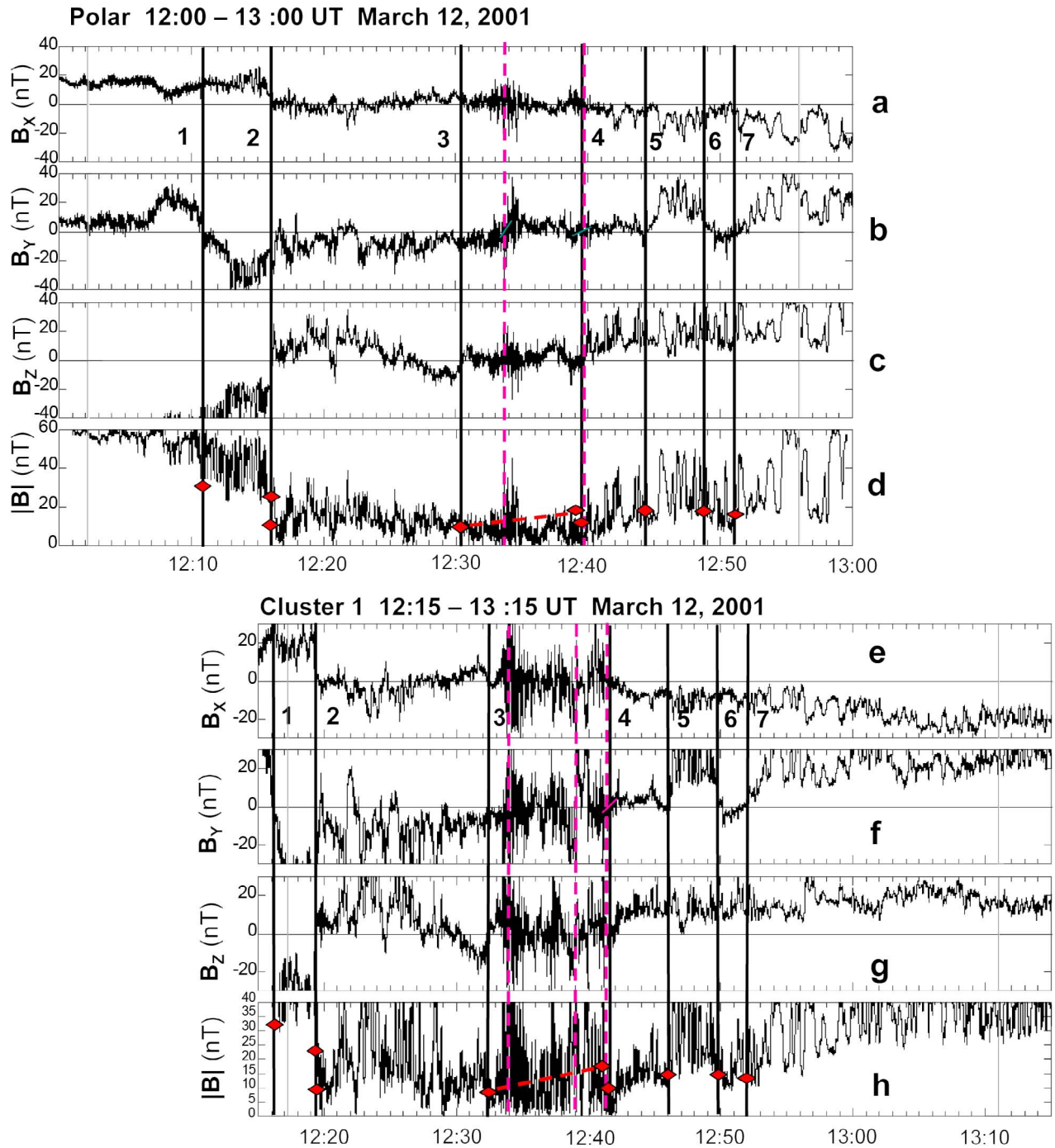
Figure 4. (a–d) The three components (X, Y, and Z) and magnitude of B measured at Polar between 1200 and 1300 UT. (e–h) The three components (X, Y, and Z) and magnitude of B measured at Cluster 1 between 1215 and 1315 UT. The data acquired before 1215 UT at Cluster are not shown, to avoid confusion, as Cluster had just entered the magnetosheath after crossing the magnetopause above the cusp [Maynard et al., 2003]. The vertical lines mark the times of the features shown in Figure 3 and itemized in Table 2. The purple dashed lines are possible candidate features to match with feature 4+ in Figure 3. Red diamonds mark |B| values found at each of the seven black lines at ACE and multiplied by 3.8 to account for the amplification of |B| while crossing the bow shock. Two values are shown on line 2 to show the steep drop in |B|. To better characterize the comparison in the interval between lines 3 and 4, a second comparison point just before line 4 was chosen. The shocked ACE values of |B| between lines 3 and 4 fall close to the red dashed line.

Table 2. Timing References

Reference Line	Event	ACE Time (UT)	Cluster Time (UT)	Difference ACE-Cluster (min)	Polar Time (UT)	Difference ACE-Polar (Polar-Cluster) (min)
1	B_Y reversal (+/−)	1108	1216.1	68.1	1211.0	63.0 (5.5)
2	B_Z reversal (−/+)	1113	1219.3	66.3	1216.1	63.1 (3.4)
3	B_Z reversal (−/+)	1117	1232.3	75.3	1230.4	73.4 (1.9)
4	B_Z, B_X reversals	1122	1242.0	80.0	1239.7	77.7 (2.3)
4+	*B_Y reversal (−/+)*	*1128.5*	*1234.0*	*[65.5]*	*1233.6*	*[65.1]*
4+	B_Y reversal (−/+)		1239.0[a]			
4+	B_Y reversal (−/+)		1241.6	[73.6]	1240.0	[72.0] (1.6)
5	B_Y reversal (−/+)	1134.1	1246.1	72.0	1244.3	70.2 (1.8)
6	*BY* drop	1145	1250.1	65.1	1248.8.	63.8 (1.3)
7	B_Y reversal (−/+)	1146.8	1251.7	64.9	1251.0	64.2 (0.7)

[a]Observable only on Cluster 1, 2, and 3.

located deep in the magnetosheath, is slightly shorter than the advection time from ACE to the bow shock. Additional time must be included for the propagation from the bow shock to Polar's location. Lag times shorter than advection times require significant IMF B_X to tilt phase planes of IMF structures [*Maynard et al.*, 2001b; *Weimer et al.*, 2002]. Second, the interval between lines 2 and 3 at Polar lasted more than 3 times longer than at ACE, indicating that the propagation time lengthened significantly. The transport time expansion increased further between lines 3 and 4 to 79 min. During this interval the IMF was dominated by B_Y with $B_X \approx 0$. Third, line 4 marks the beginning of a return to the original phase-plane tilt but with $B_X < 0$ and $B_Z > 0$. The lag time expansion reversed, so that by the time of line 6 it was nearly back to the original lag at the start of the HPS encounter.

[24] Attention is redirected to the vertical line labeled 4+ marking the only negative-to-positive reversal in IMF B_Y at ACE and Wind between lines 4 and 5. There are three possible reversals of B_Y at Cluster 1 and two at Polar (dashed and colored purple) that may correspond to line 4+ at ACE. The middle reversal appeared only at Cluster 1, 2, and 3; thus it seems to be a smaller-scale locally generated feature and not part of the large-scale interplanetary planar structure. The first was the strongest reversal at all five spacecraft locations. However, it appears to be out of place in the HPS seven-line sequence. Observation times attributed to all the purple lines are noted in Table 2 and labeled 4+. Note that the times of the first 4+ lines at Polar and Cluster 1 are nearly identical, and the propagation time from ACE is close to the originally assigned lag. This line also appears at the approximate centers of an interval in which the magnitude and variability of **B** and the magnitude of plasma density increased at both Polar and Cluster.

[25] Passage through a quasi-perpendicular bow shock (consistent with the absence of B_X in the stretched region) increases the magnitudes of **B** and n by a factor close to 4. The purely hydrodynamic calculations by *Spreiter et al.* [1966] showed that magnetosheath to solar wind density ratio is 3.8 just inside the shock, and 4.05 and 3.0 at the approximate positions of Polar and Cluster. We have multiplied the magnetic field magnitudes measured by ACE by 3.8 at each of the seven numbered lines and noted those values in Figures 4d and 4h with red diamonds. Line 2 has two values because of the large drop in |**B**|. Both lines 3 and

4 mark minima in |**B**|. An additional diamond has been added near line 4 along with a dashed red line connecting to the diamond at line 3 to show typical values between the lines based on ACE measurements. The magnitude of **B** fell below the dashed line for significant periods and for brief intervals before line 3.

[26] Figure 5a shows the magnitudes and three GSE components of ion velocities (V) measured by Polar with the seven reference lines superposed. The plasma density and β are given in Figures 5b and 5c. Figure 5d shows the ion adiabatic expansion parameter δ_i, derived from finite Larmor radius (FLR) ordering [*MacMahon*, 1965; *Scudder et al.*, 2008]. We consider its significance in the discussion below. In crossing the bow shock and propagating inward in the magnetosheath, plasma densities are expected to increase by a factor of 4.05, as mentioned above [*Sprieter et al.*, 1966]. Red diamonds, marking expected density increases with respect to ACE measurements, were usually in good agreement with Polar measurements. Between lines 2 and 3 the density was ~80 cm^{-3}. After 1230 UT (line 3) it increased rapidly to 140 cm^{-3}. This high-density interval is not expected from the ACE data. This peak occurred near the time of the first purple 4+ line (Table 2). Note that β_i was large, varying between 10 and 1000. After the HCS passage (lines 1 and 2), the velocity components were relatively constant, with positive V_{iZ} (~85 km s^{-1}) and negative V_{iX} (approximately −60 km s^{-1}) dominating, while V_{iY} remained near zero. The exception to this occurred near 1234 UT (purple line) when |**V**$_i$| and V_{iZ} decreased. This corresponds in time to that of the first 4+ event listed in Table 2.

[27] Figure 6 compares the three components of the perpendicular (red), parallel (blue), and total (orange) ion velocity (Figures 6a, 6c, and 6e) to the ($\mathbf{E} \times \mathbf{B}$)/$B^2$ convective velocity ($\mathbf{V_C}$) (Figures 6b, 6d, and 6f). The three components of **E** were derived from measurements by Polar's two double probes in the spin plane, assuming that $\mathbf{E} \cdot \mathbf{B} = 0$. Data are plotted as functions of time from 1219 to 1244 UT. This corresponds to the interval marked by a horizontal bar in Figure 5a. On both sides of this interval the electric field sensors occasionally experienced episodes during which the sensor preamplifiers went into oscillation, corrupting the measurements. Also, $\mathbf{V_C}$ data are not plotted at times when **B** was aligned closer than 15° to the spin plane. This limits the multiplicative factor to 3.7 on errors in the spin plane measurements from affecting the calculation of the spin
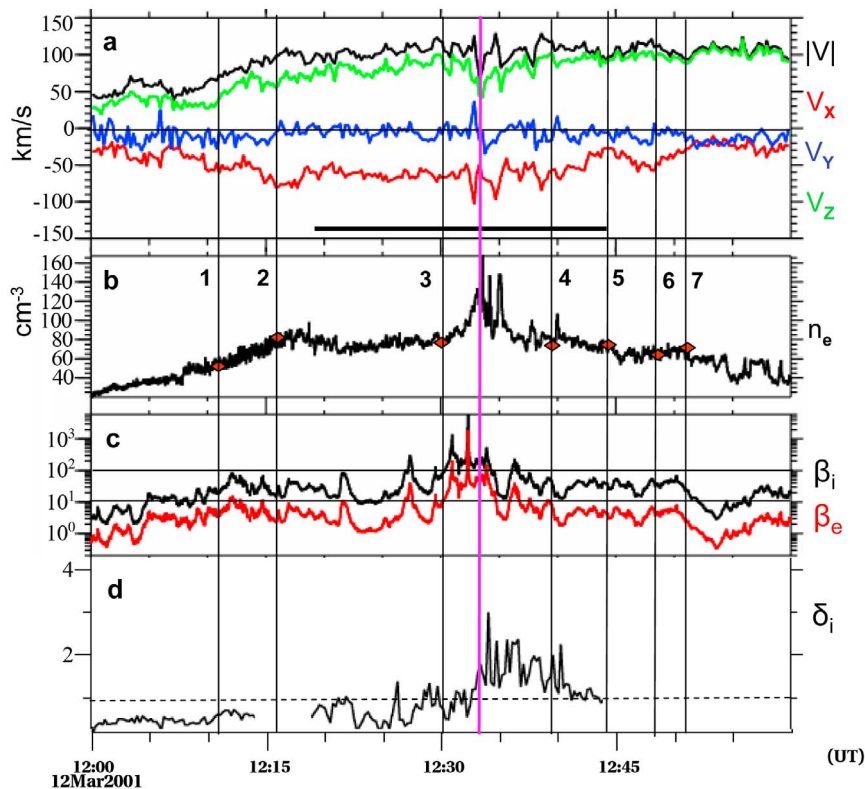
Figure 5. (a) The magnitude and three GSE components (X, Y, and Z) of the ion velocity (V) measured by Polar. (b) The ion density measured by Polar. (c) The ion (β_i) and electron (β_e) beta values. (d) The ion delta (δ_i) values determined from Polar measurements (see section 6.2). The seven black reference lines are repeated from Figures 3 and 4. The purple line represents the time of line 4+ (as argued for in section 6.1). Red diamonds at each black line mark the values at ACE multiplied by 4.05. This increased scaling factor reflects the higher magnetosheath compression found in hydrodynamic calculations of *Spreiter et al.* [1966]. The black bar in Figure 5a marks the interval depicted in Figure 6.

axis component by enforcing $\mathbf{E} \cdot \mathbf{B} = 0$. Lines 3 and 4 fall within the plotted interval of good data retrieval. The $\mathbf{E}$ field values (not shown) were small and variable, as were the magnetic field components (Figure 4). As a result the convective velocity components appear noisy. $V_{i\perp X}$ (the red trace) in Figure 6a and V_{CX} in Figure 6b show good agreement. However comparisons along the other two axes reveal differences. The Y components in Figures 6c and 6d have regions of similarity and others where they differ. The most consistent differences are between $V_{i\perp Z}$ and V_{CZ} found in Figures 6e and 6f up through 1234 UT. From there to 1240 UT there is a semblance of tracking. After 1240 UT $V_{i\perp Z}$ is near zero, while V_{CZ} is slightly negative. The ion velocity is nearly parallel to B (blue trace). We will investigate this further in the discussion after presenting the Cluster data.

[28] Cluster 3 data are presented in Figures 7 and 8. The black and red vertical reference lines in Figure 4 and Table 2 are also shown in Figures 7 and 8. Figures 7a–7f display 4 s averaged values of the GSE components and magnitude of $\mathbf{B}$, and ion densities and temperatures between 1215 and 1315 UT. Red diamonds in Figures 7d and 7e represent corresponding quantities measured by ACE, multiplied by 3.8 (Figures 3 and 4). Figures 8a–8c present the three GSE

components of the calculated $(\mathbf{E} \times \mathbf{B})/B^2$ velocity over the same interval derived from spin fit electric field data (assuming $\mathbf{E} \cdot \mathbf{B} = 0$). Data gaps appear at times when $\mathbf{B}$ was within 15° of the spin plane, eliminating any significant errors stemming from enforcing $\mathbf{E} \cdot \mathbf{B} = 0$. Prior to 1240 UT the convective velocity at Cluster was similar to that measured at the location of Polar (Figure 6). The measured ion flow velocity ($\mathbf{V}_i$) components and magnitude are displayed in the black traces of Figures 8d–8g. Overlaid in blue in Figures 8d–8g are the values of $\mathbf{V}_i$ perpendicular to $\mathbf{B}$. Figure 8h displays the magnitude of $\mathbf{V}_i$ parallel to $\mathbf{B}$.

[29] Note that in addition to the low-magnitude extremely variable $\mathbf{B}$ and the very high density, there are significant changes in the magnitude and components of $\mathbf{V}_i$, especially between 1233 and 1242 UT (lines 3 to 4). Excluding the interval bound by lines 3 and 4, typical values for V_{iY} and V_{iZ} are 37 and 86 km s^{-1}, respectively. The V_{iX} started near -60 km s^{-1} and gradually became more negative with time as the spacecraft moved deeper into the magnetosheath. Between lines 3 and 4 $\mathbf{V}_i$ components change dramatically. Near the time of the first of the purple 4+ lines V_{iY} decreased to near zero as V_{iZ} increased. At this time the local density grew to >140 cm^{-3}, the ion temperature decreased, $|\mathbf{V}_i|$ peaked at 180 km s^{-1} and V_{iY} increased to 90 km s^{-1} before
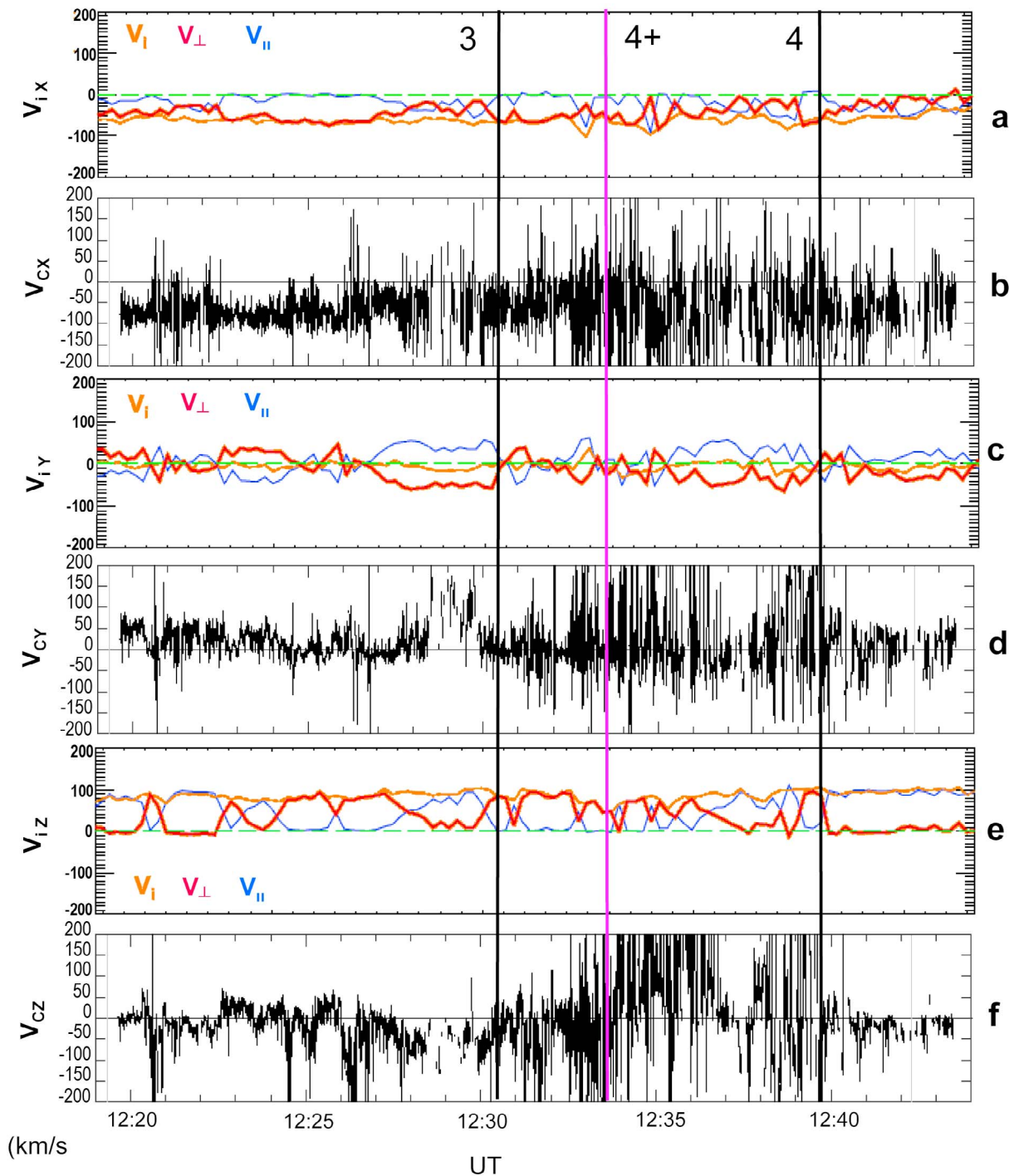
Figure 6. (a, c, e) The three GSE components (X, Y, and Z) of the ion velocity (V_i, orange) measured at Polar, with their perpendicular (red) and parallel (blue) parts. (b, d, f) The three components (X, Y, and Z) of the convective velocity (V_C) determined from the electric and magnetic field measurements ($\mathbf{E} \times \mathbf{B}/B^2$). The interval is that marked by the black bar in Figure 5a (see section 5).

falling to zero at the time of the second purple 4+ line. Variability appeared in the other components. Note that the perpendicular components of $\mathbf{V}_i$ are much more variable than $\mathbf{V}_i$ itself, as might be expected from the highly variable $\mathbf{B}$, suggesting that significant parallel velocity components ($\mathbf{V}_i - \mathbf{V}_{i\perp}$) were present for relatively long inter-

vals. The magnitude of the parallel velocity in Figure 8h shows similar but opposite variations with that of $|\mathbf{V}_{i\perp}|$ in Figure 8g.

[30] Blue traces in Figures 8d–8f ($V_{i\perp}$) have similarities to the convective velocities calculated from $\mathbf{E} \times \mathbf{B}/B^2$ in Figures 8a–8c, as anticipated. The components of $\mathbf{V}_i$ (black
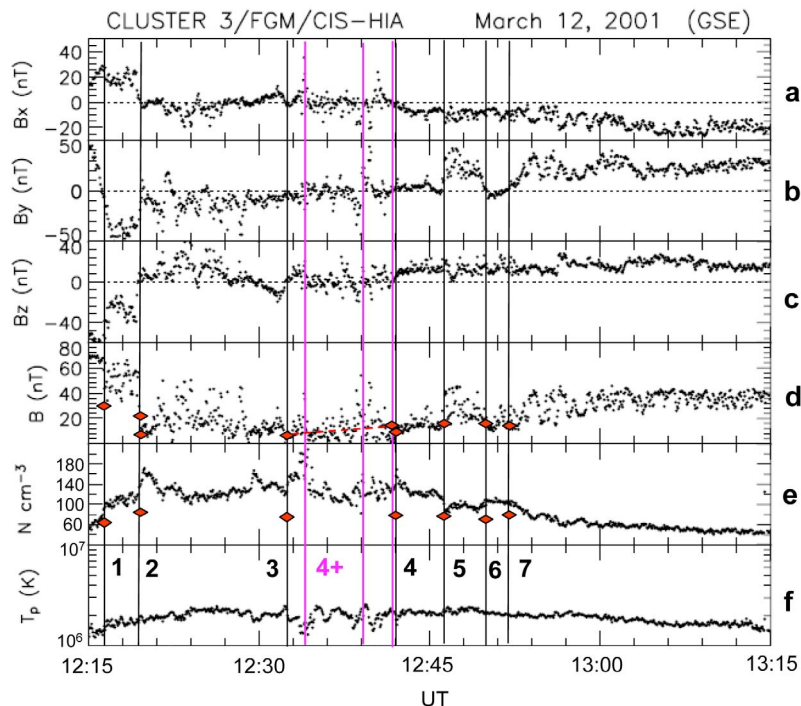
Figure 7. Four-second averaged data from Cluster 3 in GSE coordinates: (a–d) the three components (X, Y, and Z) and magnitude of B and (e–f) the ion density (N) and temperature (T). The seven black lines are repeated from Figure 4. Red diamonds in Figure 7d represent the shock solar wind values using a multiplicative factor of 3.8. The same factor was used to obtain red diamond–associated values in Figure 7e. The pure hydrodynamic calculations of *Spreiter et al.* [1966] require a lower factor to account for the high latitudes of Cluster. Three reversals of B_Y, which are possibilities for line 4+, are identified by purple lines (see Table 2).

traces) show less variation and are stronger than the convective velocities, indicating significant parallel velocity components. After 1241 UT V_{CY} (and $V_{i\ \perp Y}$) turned negative, unlike V_{iY} (black trace). The parallel velocity in this period is dominating $\mathbf{V}_i$, as can be seen in comparing Figures 8g and 8h.

[31] A minimum variance analysis, performed on Cluster 3 magnetic field data over the interval 1215 to 1315 UT (Table 1) found a normal vector direction within 1.4° of that calculated in the corresponding hour interval using ACE data. Figure 9 presents the components of $\mathbf{B}$ and $\mathbf{V}_i$ in the normal (k) direction, the angle between $\mathbf{B}$ and $\mathbf{V}_i$, and the magnitude of $\mathbf{V}_i$. Vertical lines from Figure 4 are repeated. Component B_k (Figure 9a) increased in variability and amplitude during the interval between lines 3 and 4. The largest variations in B_k are near the first two red lines. While the average of B_k over the minimum variance analysis interval (B_N) of −1.2 nT at Cluster is similar to the normal component at ACE, it is not statistically significant in the Cluster analysis because of the enhanced variability in $\mathbf{B}$.

[32] The velocity component normal to the front (V_k) was generally negative and about 50 km s^{-1} (Figure 9b). Each of the seven lines provides an opportunity to identify the timing of the associated feature at each of the four Cluster spacecraft. Following triangulation procedures described by *Russell et al.* [1983] we determined the velocities of features at each of these times. The results are given in Table 3. We have overlaid the component along the minimum variance normal of these values on the V_k trace in Figure 9b using red diamonds. The agreement is good. The implication is that the identified features were moving in and with the front normal. The large negative jump in V_k occurred near 1234 UT, the time of the first 4+ line (see also Table 2).

[33] The primary HCS layer impinged on the magnetosphere-magnetosheath system between 1215 and 1223 UT. In this period the shear angle between $\mathbf{B}$ and $\mathbf{V}_i$ rotated from strongly antiparallel to perpendicular and then toward parallel (Figure 9c). In the subsequent passage of the HPS, the shear angle oscillated wildly about 90° (because of the large variability in $\mathbf{B}$) before settling out in a direction favoring parallel. Thus over a large portion of the HPS crossing, the parallel component of the velocity was as large as, or larger than, the perpendicular component.

[34] The sonic, Alfvén, magnetosonic, and measured speeds, along with their corresponding Mach numbers, and plasma β_i, calculated using Cluster 3 data, are shown in Figure 10. The vertical lines and the extent of the HPS are repeated. The most striking features are very high β_i values (Figure 10i) that consistently exceeded 100 and approached 10,000. Simultaneously, Alfvén speeds (V_A) were very low (Figure 10b) throughout the magnetic hole region, reaching below 20 km s^{-1}. Consequently, measured ion velocities are consistently super-Alfvénic with the Alfvénic Mach numbers (Ma_A) ranging up to 100. The sonic and magne-
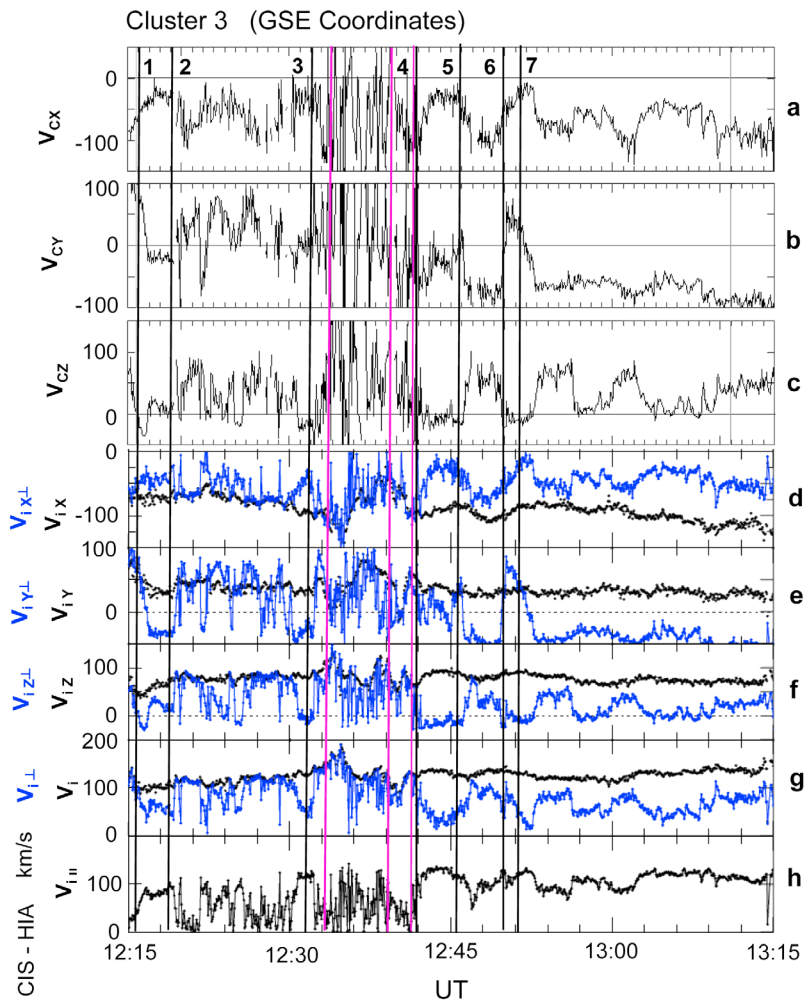
Figure 8. (a–c) Three GSE components (X, Y, and Z) of the convective velocity (V_C) calculated from $\mathbf{E} \times \mathbf{B}/|\mathbf{B}|^2$ using spin-averaged values of the Cluster 3 measured electric and magnetic fields. (d–g) The three components and magnitude of the ion velocity (V_i) measured at Cluster 3 (black) and the perpendicular parts of those velocities (blue). (h) The magnitude of the part of the ion velocity parallel to $\mathbf{B}$. The vertical lines are repeated from Figure 7.

tosonic velocities (calculated using a gamma of 5/3) are nearly identical and ranged between 200 to 260 km s^{-1}.

6. Discussion

[35] Having Polar and the four Cluster spacecraft in the magnetosheath as the HPS-HCS passed by Earth provided an opportunity to study the effects of high-β plasmas on the dynamics of the dayside magnetosheath and magnetosphere. This section has three parts. We first consider the magnetic structures in the magnetosheath associated with the magnetic hole embedded in the HPS-HCS. Second, we comment on the significance of the observed magnetic variability and ion dynamics. Finally, we use MHD simulations to explore the range of coupling available to the magnetosphere under low |$\mathbf{B}$| conditions, with the observed mix of hydrodynamic and magnetohydrodynamic forcing.

6.1. Magnetosheath Consequences of the HPS-HCS Magnetic Hole

[36] Data presented in Figures 2 and 3 demonstrated that ACE and Wind crossed the heliospheric current and plasma sheets between 1100 and 1200 UT (time at ACE). The HCS and HPS are large-scale planar structures. Despite their Y_{GSE} separation of ~124 R_E, minimum variance analyses of ACE and Wind magnetic field data (Table 1) showed that the normal direction at both spacecraft was ~30° from the X_{GSE} axis. This large-scale planarity does not preclude variations in the normal directions and the HPS thickness due to waves and other perturbations. This is illustrated by the ~20° angle between the normal vectors from ACE and Wind and the shorter duration of the HPS passage at Wind.

[37] The HCS separates regions of opposite IMF polarity, away from the Sun north of the HCS and toward the Sun south of it [e.g., *Kivelson and Russell*, 1995]. In the present case the change in IMF at line 2 is consistent with a current in the $-Y$ direction that initiates a rotation as ACE moved
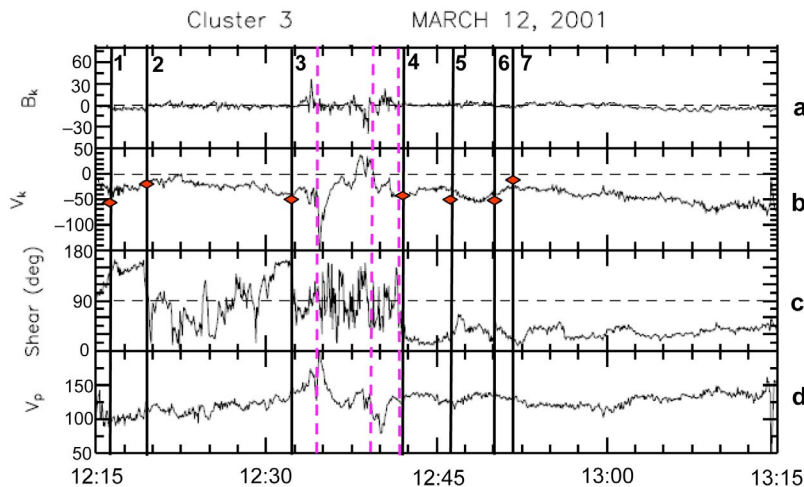
Figure 9. Cluster measurements transformed to minimum variance coordinates (i, j, and k). (a–b) The components of **B** and **V** along the direction of minimum variance (k). (c) The angle between **B** and **V**, and (d) the magnitude of **V**. The reference lines from Figures 4 and 7 are repeated. At each of those 7 lines we triangulated the velocities of associated feature through the Cluster constellation (see Table 3). The magnitudes of the triangulated velocities along the minimum variance normal are shown by the red diamonds in Figure 8h. The 3 dashed purple lines representing possibilities for 4+ are repeated from Figure 7.

from south to north of the HCS (Figure 3). Note that the rotation of IMF B_X from toward the Sun to away from the Sun was not completed until after line 4, nine minutes later. The 9 min of nearly 0 B_X, between initial (line 2) and final contacts (line 4) is consistent with the satellite having been embedded within the basic heliospheric current sheet of finite thickness separating the southern and northern solar hemispheres. Prior to line 2 a rotation of the IMF, dominated by a change in B_Y, occurred at line 1. This served to rotate the IMF in the ecliptic plane close to the Parker average spiral angle of ~45°. After line 4, a reversal of IMF B_Y is seen at line 4+ completing the IMF direction change from this HCS crossing from toward to away, oriented approximately along the Parker spiral angle. At ACE this last major direction shift was near the center of the magnetic hole of the HPS. At Wind there was a last B_Y reversal near the same lagged time and a previous reversal between lines 3 and 4 determined from the ACE data. The earlier reversal occurred near the center of, and the last reversal was nearer the end of, the shortened HPS at Wind.

[38] A source of localized, small-scale perturbations to the HPS and HCS is the Earth's magnetosphere and associated bow shock which act as obstacles. In the magnetosheath behind the bow shock plasma velocities are slowed, locally distorting the large-scale planar structure. However, on the 1 hour time scale of the minimum variance analyses, the orientation of the structure in the dayside magnetosheath was similar to that observed upstream at ACE. The Cluster normal was within 1° of that at ACE, while the Polar normal less than 13° away from that at ACE, but only 20° tilted from the X_{GSE} axis.

[39] Within the HPS, but away from the principal current sheets, the magnetic field was small and the density high, leading to β_i values at ACE between 1 and 10 (Figure 3i). This compares with typical solar wind β values at 1 AU, which are of order 1. The interaction of this high-β region with the bow shock led to remarkable effects in the magnetosheath. The most striking feature was that within the magnetosheath magnetic field magnitudes were significantly weaker than expected for the shocked solar wind. For brief intervals they were even less than the measured solar wind values. At Polar, β_i values were consistently above 10 and reached over 1000 (Figure 5c), while at Cluster the

Table 3. Triangulation Results

Reference Line	Event	Cluster 3 Time UT	Velocity (km/s)	GSE Direction Cosines		
				X	Y	Z
1	B_Y reversal (+/−)	1216:05.2	64.2	−0.8510	0.2766	−0.4467
2	B_Z reversal (−/+)	1219:19.3	24.2	−0.8879	0.2032	−0.4138
3	B_Z reversal (−/+)	1232:16.5	54.4[a]	−0.9029	−0.0167	−0.4294
4	B_Z, B_X reversals	1242:12.9	48.0	−0.7940	0.2643	−0.5473
5	B_Y reversal (−/+)	1246:05.4	53.6	−0.9395	0.0595	−0.3373
6	B_Y drop	1250:05.1	58.3	−0.8441	−0.2998	−0.4445
7	B_Y reversal (−/+)	1251:42.8	17.1	−0.7766	0.0905	−0.6234
(4+)	increase in **|B|**	1233:41.3	148.0	−0.4900	0.3124	0.8143

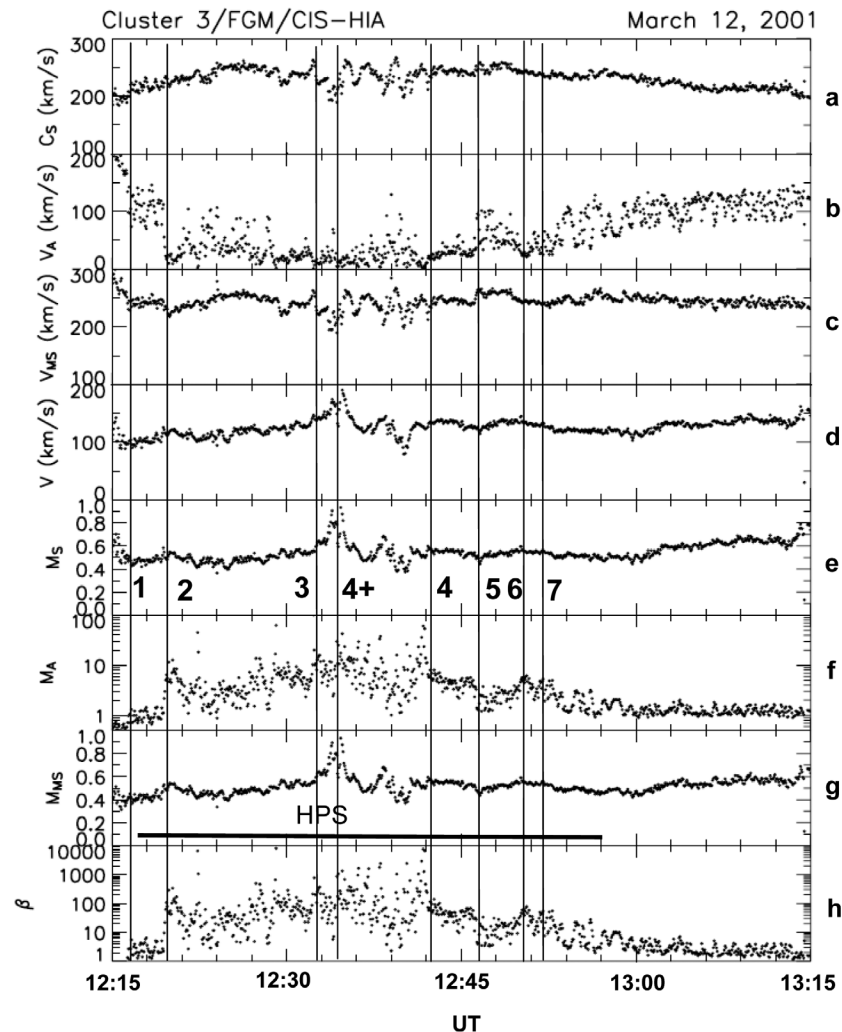[a]Polar replaced Cluster 4 in the triangulation because of a data gap.

Figure 10. (a–d) Calculated sonic (C_S), Alfvén (V_A), and magnetosonic (V_{MS}) speeds, and measured ion velocities (V) determined from Cluster 1 data. (e–g) The respective sonic, Alfvénic, and magnetosonic Mach numbers, and (h) β_i. The extent of the HPS is shown by the black line in Figure 9h.

β_i values were consistently above 100 and approached 10,000 (Figure 10i).

[40] Several factors may be involved. We first consider the nearly 9 min interval at ACE between reference lines 2 and 4 (Figure 3) during which B_X was nearly zero in the HCS. Before (after) this interval B_X was significant and positive (negative), while B_Z was negative (positive). We have noted that the 9 min interval between lines 2 and 4 expanded to 22.7 min at Clusters 1 and 3 and 23.6 min at Polar (Table 2). While the lag times from ACE to Cluster and Polar were less than the advection time to the bow shock at line 2, they increased by ~14 min to values longer than the advection time at line 4. They then returned to values near the original lag time by the time of line 6 as B_X became more negative. *Maynard et al.* [2001b] and *Weimer et al.* [2002] attributed such lag time changes to rotations in the orientation of tilted phase plane containing interplanetary **E** and **B**. Using data from four satellites in the solar wind, *Weimer et al.* [2002] showed that the tilt could rotate significantly on time scales of tens of minutes as B_X changed. Changes in tilt result in a spreading and/or com-

pression of the local IMF as illustrated schematically by *Maynard et al.* [2006, Figure 3]. We thus believe that magnetic flux expanded between lines 2 and 4 in the extended HCS region and recompressed between lines 4 and 6. Considering that this is a large-scale planar structure, the dilation of the time difference between lines 2 and 4 by more than a factor of 2 at Cluster, compared with ACE, implies a spreading of the magnetic field (or a decrease in |**B**|). We thus attribute the low magnetic field values between lines 2 and 4 in part to the expansion of the interval from the changing phase plane orientation. After line 4 the lag time recompressed while |**B**| remained at or above the shocked ACE values (Figure 4).

[41] Above we marked a reversal of IMF B_Y at ACE as line 4+. We tentatively suggest that it acts as a boundary layer adjustment on exiting the HCS and the HPS similar to the B_Y reversal at line 1, prior to the large HCS current layer at line 2. The problem is to identify its counterpart at Cluster and Polar. Three negative to positive reversals are identified with purple lines within the Cluster 1 data (Figure 4f), and two of them appear in the Polar data stream (Figure 4b).
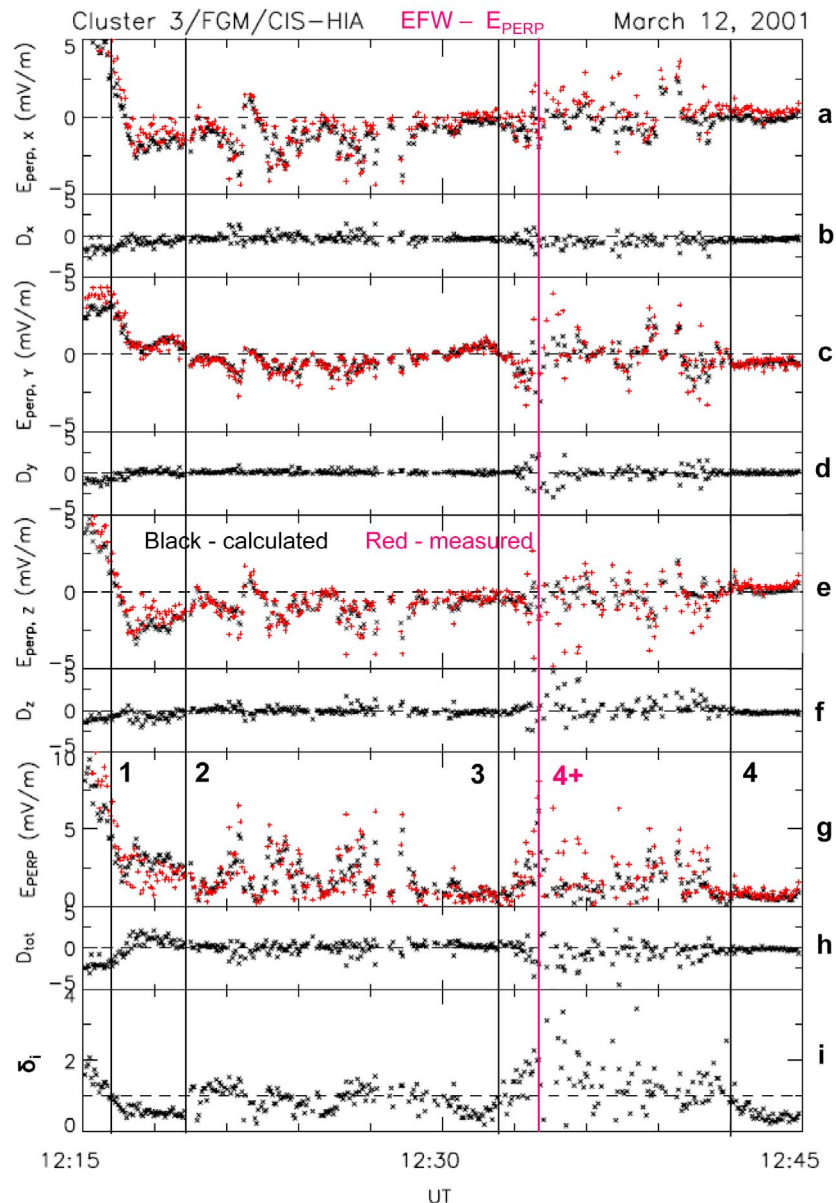
Figure 11. (a, c, e, g) The three components and magnitude of the perpendicular electric field measured by the Cluster double probe instrument (EFW) (in red) and calculated from $-\mathbf{V}_i \times \mathbf{B}$ (in black). The measured electric field values are from spin fits of the 1–2 dipole pair data assuming $\mathbf{E} \cdot \mathbf{B} = 0$. (b, d, f, h) Differences between the measured electric fields and those calculated from $-\mathbf{V}_i \times \mathbf{B}$. (i) The value of the quantity δ_i (see section 6.2 for definition); values of 1 or greater indicate demagnetization of the ions.

However, none of the B_Y reversals occurred significantly after line 4. The times of the reversal are listed in Table 2. We ruled out the middle B_Y reversal at Cluster 1 as being a large-scale driven feature since it was seen by neither Cluster 4 nor Polar. Thus its scale size is ≤ 600 km, the typical interspacecraft separation of Cluster spacecraft. The last reversal was very weak at both Polar and Cluster and occurred at or just before line 4. It may be that the expansion of the lag time between lines 2 and 4, and subsequent compression, served to combine the B_Z reversal of line 4 with the B_Y reversal of line 4+ (at ACE) as one feature when it reached Polar and Cluster. The strongest B_Y reversal occurred at the time of the first 4+ line. It is clearly a sep-

arate feature, but it occurred out of sequence when compared with line 4+ at ACE. In the following paragraphs and in the Cluster and Polar figures where only one line 4+ is noted, it refers to this line (bold in Table 2). We will come back to the third line later.

[42] Line 4+ has several interesting properties. First, the lag between 4+ events at Polar and at Cluster was only 0.4 min. Features on either side had lags of 1.9 and 2.3 min. The average magnetic field and density increase and then decrease, peaking at both locations at the time of line 4+. Such correlated variations are characteristic of magnetosonic fast waves. Recall that the sonic and magnetosonic velocities were virtually the same because of the small Alfvén

velocity. However, ion acoustic waves involve no change in |B| and in magnetized plasmas they propagate along **B**. A magnetosonic slow-mode interpretation is also ruled out because the |B| and density variations would have been anticorrelated.

[43] We were able to identify the arrival of a magnetic field increase at all four Cluster spacecraft. Triangulation revealed a velocity of 148 km s^{-1}. Subtracting the velocity for line 3 given in Table 3 (the velocity of the planar structure) set the triangulated velocity into the rest frame of the HCS-HPS front. In this frame of reference the phase velocity was 159 km s^{-1}, predominantly in the Z direction and 86° from the direction of the magnetic field at the upward ramp onset. This is comparable to the magnetosonic velocity of ~200 km s^{-1} and identifies the increase as a fast compression wave. Figures 8d–8h provide the parallel and perpendicular components of ion velocities, which may be compared with the Alfvén speeds (V_A) and Alfvén Mach numbers (Figures 10b and 10f) during the interval spanned by lines 1 to 4. Note that near the time of line 4+ the velocity was primarily perpendicular to **B**, consistent with the fast wave interpretation (Figure 8g). After the peak in density and magnetic field at line 4+, both quantities decreased consistent with a fast rarefaction wave, likely a reflection of the incident wave from the magnetopause. Because of the intense higher-frequency variations and a data gap, we were unable to identify unambiguously start times of the rarefaction wave at the locations of all four spacecraft as is needed to estimate its phase speed via triangulation. Fast waves mediate pressure changes and have been observed in the magnetosheath consequent to directional discontinuities with associated solar wind density changes impacting the bow shock [*Maynard et al.*, 2007, 2008]. No associated density change or dynamic pressure change is obvious in the ACE data associated with the ACE 4+ B_Y reversal. Line 3 at ACE is near the end of an upward trend in both ion temperature and ion velocity (Figures 3c and 3b) and the start of a slow downward trend in density (Figure 3a).

[44] Data plotted in Figures 4, 5, and 8 indicate other noteworthy variations at the time of line 4+. They include large variations in |B| at both spacecraft. At Polar both |V| and V_Z decreased, while at Cluster they both increased. At ACE, Cluster, and Polar the line 4+ event occurred near the center of the HPS. The lag time between ACE 4+ and Polar and Cluster was 65 min. This is comparable to the lag times before and after the stretching and compression of the magnetic field due to changes in the phase-plane tilt but not to the lag times for lines 3 and 4. The fast-wave-dominated structure around the time of line 4+ served to compress and then expand the magnetic flux and provide a further reason for the low magnetic field values observed on either side of it. However, identifying line 4+ as a fast wave out of sequence with the other IMF features negates our supposition that it was a boundary layer feature to the HCS-HPS. This makes the last of the three original possible negative-to-positive transitions of B_Y the most likely to be associated with line 4+ at ACE.

6.2. Magnetic Variability and Ion Dynamics

[45] Large variations in **B** occurred throughout the interval between lines 2 and 4 but are especially evident near the time of line 4+. *Parks et al.* [2007] detected solitary non-linear electromagnetic pulses (δ**B**/**B** ≫ 1) in the current sheet portion of the Earth's magnetotail during intervals of high-β, super-Alfvénic ion flow with $V_\perp > V_A$ ($Ma_{A\perp}$ ~4). They interpreted observed pulses as steepened ion cyclotron waves within the current layer and steepened Alfvén waves in the boundary layer. The yet to be identified responsible mechanisms are nonlinear and involve high-β plasmas in which the ions do not follow simple Larmor motions about drift guiding centers. However, the electrons are still tied to the magnetic field. While the events described here and by *Parks et al.* [2007] are in very different regimes and have different origins, they manifest a number of similarities.

[46] From Figures 8g and 10b we see that the perpendicular velocity was larger than the Alfvén speed over most of the interval. In the vicinity of line 4+, **V** rotated from largely parallel to primarily perpendicular to **B**, consistent with our fast-wave interpretation, and then back to mostly parallel. During this interval $V_\perp$ >20 V_A, thereby meeting one of the conditions for nonlinear growth cited by *Parks et al.* [2007]. After line 4, V_A increased and approached $V_\perp$. The variability of the magnetic field decreased significantly after line 4.

[47] A second criterion used by *Parks et al.* [2007] is that individual ions do not follow simple superposed Larmor and guiding center motions. The Larmor radius of 10 keV ions in a 2 nT magnetic field is >7000 km. Large variations in the magnetic field shown in Figure 4 between lines 3 and 4 occur on time scales of 1 to 10 s, or on spatial scales of 100 to 1000 km, considering an average ion velocity of 100 km s^{-1}. The magnitudes of the variations are greater than those of the average magnetic field, and their temporal scale is also much less than the 32 s needed to complete one gyrocycle in a 2 nT magnetic field. The measured velocity components are much smoother than their $V_\perp$ counterparts. On both spatial and temporal scales Cluster and Polar measurements indicate that locally observed ions were demagnetized.

[48] Our contention that the ions are at times demagnetized and dominated by hydrodynamic forces is also supported by comparison of ion velocities ($V_{i\perp}$) measured by Polar (Figures 6a, 6c, 6e) with the convective velocities ($\mathbf{V}_C = (\mathbf{E} \times \mathbf{B})/|\mathbf{B}|^2$) (Figures 6b, 6d, 6f). Purely hydrodynamic flow should fan away from the subsolar magnetopause (see dotted arrows in Figure 1). In addition to a $-V_{iX}$, this would produce positive V_{iY} and V_{iZ} at the locations of Polar and Cluster. However, if the ions are tied to the field lines, their velocities would differ from the convective velocity only in regions of electric current flow. We argued above that the current from the HCS is in the $-Y$ direction. This should be the primary component of current driven differences between $\mathbf{V}_{i\perp}$ and $\mathbf{V}_C$. There are periods, especially between 1220 and 1230 UT, where $V_{i\perp Y}$ is more negative than V_{CY}. However, comparing $\mathbf{V}_{i\perp}$ and $\mathbf{V}_C$ at Polar using Figure 6, we see that the largest differences are between $V_{i\perp Z}$ and V_{CZ} and not in the Y components. The significant differences between $\mathbf{V}_{i\perp}$ and $\mathbf{V}_C$ indicate the ion motions are dominated by inertia and flow away from the stagnation point at the nose. That they do not follow simple guiding center motion is evidence for demagnetization.

[49] At Cluster the comparison of $\mathbf{V}_{i\perp}$ and $\mathbf{V}_C$ (Figure 8) shows many similarities but also differences. For instance, near 1230 UT $V_{i\perp Y}$ is negative while V_{CY} is near zero. Near

line 4 the difference was positive. There are varying differences in component amplitudes at many times. We suggest that at Cluster both hydro and magnetic forcing competed for control of the ion motion in ways that depended on the instantaneous magnitude of **B**.

[50] To make the comparison more quantitative, Figure 11 plots the components and magnitude of the perpendicular electric field calculated from $-\mathbf{V}_i \times \mathbf{B}$ using Cluster 3 CIS-HIA and magnetometer data (in black) overlaid by the measured electric field using spin fit data from sensors 1 and 2 and the assumption of $\mathbf{E} \cdot \mathbf{B} = 0$ (in red). An extensive error analysis was performed. Even with the worst multiplication factor from the $\mathbf{E} \cdot \mathbf{B}$ assumption, we conservatively expect the X and Z electric field components are accurate to better than ± 0.5 mV m^{-1} and the Y component to better than ± 1 mV m^{-1}. Considering the errors in the velocity and magnetic field measurements, the total error in $-\mathbf{V}_i \times \mathbf{B}$ calculations is approximately ± 0.1 mV m^{-1}. If the ions are convecting with **B,** the perpendicular electric field calculated from the ion velocity should be identical to the measured perpendicular electric field. Differences are a measure of polarization electric fields arising from unequal electron and ion motions, since the electrons are still tied to the magnetic fields. The differences for each component and the magnitudes are displayed under their respective plot. Note that the largest differences occurred between lines 3 and 4. Time-varying electric and magnetic fields create small imbalances when the electrons are tied to the fields and ions are not. As a consequence, ambipolar electric fields develop to help regulate the particle motions to conform to the dominant hydro forcing. Figure 11 quantifies the existence and magnitude of these fields at Cluster 3.

[51] The adiabatic expansion parameter is $\delta_{i,e} = \rho_{i,e}/L$. Here symbols $\rho_{i,e}$ and L represent the thermal gyroradius of either ions or electrons and the dominant spatial scale lengths of their variations, respectively. As such, $\delta_{i,e}$ is a measure of how well a species is tied to magnetic field lines. If $\delta_{i,e} \ll 1$ for ions and electrons, both are well described by guiding center theory, and the MHD approximation to the generalized Ohm's law applies. Conversely, a particle species is said to be demagnetized if $\delta_{i,e} > 1$ [*MacMahon*, 1965; *Vasyliunas*, 1975; *Scudder et al.*, 2008]. The simultaneous demagnetization of both ions and electrons is a signature of electron diffusion regions near magnetic merging sites. This was a point of interest in the work by *Scudder et al.* [2008]. In the present case, electrons detected at the location of Polar (not shown) were far from meeting the demagnetization criterion. Hence this is not a magnetic merging event. Rather, our present focus is on δ_i. The appropriate scale for the Hall or $\mathbf{J} \times \mathbf{B}$ term being important in the generalized Ohm's law is the ion inertial scale size, $L = c/\omega_{pi}$, where ω_{pi} is the ion plasma frequency and c is the speed of light [*Vasyliunas*, 1975]. Using the ion inertial scale size as L, *Scudder et al.* [2008] showed that $\delta_i = \beta_{\perp i}^{1/2}$. With the measured β_i typically over 100 and sometimes exceeding 1000 between lines 2 and 4 (Figure 5c), $\beta^{1/2}$ was >10, indicating that ion gyroradii exceeded the ion inertial scale by more than a factor of 10.

[52] On the basis of FLR-ordering considerations, *Scudder et al.* [2008] also demonstrated that δ is more accurately connected to the ratio of the perpendicular elec-

tric to magnetic force experienced by a thermal particle in the fluid's rest frame as

$$\delta_{i,e} \equiv \frac{\left| E_\perp + U_{i,e} \times B \right|}{w_{\perp i,e} B} \tag{1}$$

where

$$w_{\perp i,e} \equiv \sqrt{2k T_{\perp i,e}/m_{i,e}}$$

represents the mean thermal speeds of ions and electrons. Figure 5d displays δ_i calculated using this formula based on Polar measurements (excluding intervals when electric field preamps experienced oscillations). The δ_i exceeded 1 for most of the interval between lines 3 and 5 and was of the order 2 between lines 3 and 4. We also used Cluster 3 data to calculate δ_i with this formula. Results shown in Figure 11i are very similar to those in Figure 5d obtained using Polar data. There are long stretches where δ_i is near 1. However, especially between lines 3 and 4, δ_i was often >2.

[53] We have also used δ_i to back out scale lengths implied by the FLR-ordering condition. Taking the values of $T_i = 2 \ 10^6$ K, $B = 8$ nT, $n = 140$ cm^{-3}, and $\beta = 100$, as measured by Cluster at the time of line 3 (Figures 7 and 10), we determine the ion gyroradius to be 167 km and the ion inertial length to be 19.2 km. Figure 11i shows that δ_i was ~1 at that time. The FLR scale length (L_{FLR}) is ρ_i/δ_i, or 167 km in this case, i.e., ~8 times more stringent than using the ion inertial length as a scale for ion demagnetization. Meeting the FLR-based scale clearly indicates that ions were demagnetized during the passage of the HCS-HPS structure and simply could not follow combined Larmor and guiding-center drift motions. This also implies that pressure gradient forces are important in the generalized Ohm's law and have scale sizes that approach or are smaller than ρ_i. Under such conditions a gyrotropic pressure tensor cannot be maintained.

[54] We conclude that in addition to the above suggested nonlinear processes, the observed ion flow is dominated by pressure gradients away from the stagnation point. The rapidly varying, small magnetic field has little influence on the flow vector, other than our calculated separation into perpendicular and parallel components.

6.3. Hydrodynamic and Magnetohydrodynamic Coupling to the Magnetosphere

[55] In the MHD and gas-dynamic regimes, coupling to the magnetosphere mainly proceeds through the high-latitude [*Dungey*, 1961] and low-latitude [*Axford and Hines*, 1961; *Lotko et al.*, 1987] boundary layers, respectively. A readily observable indicator of such a regime transition occurs in the character of ionospheric plasma convection. Both coupling mechanisms produce two-cell convection patterns in the high-latitude ionosphere [e.g., *Heppner and Maynard*, 1987]. However, MHD coupling results in anti-sunward convection on open field lines across the polar cap. In the case of hydrodynamic forcing, antisunward convection is due to coupling through the LLBL and is on closed field lines that map to the dawn and dusk flanks of the polar cap. To illustrate how MHD and hydrodynamic forcing
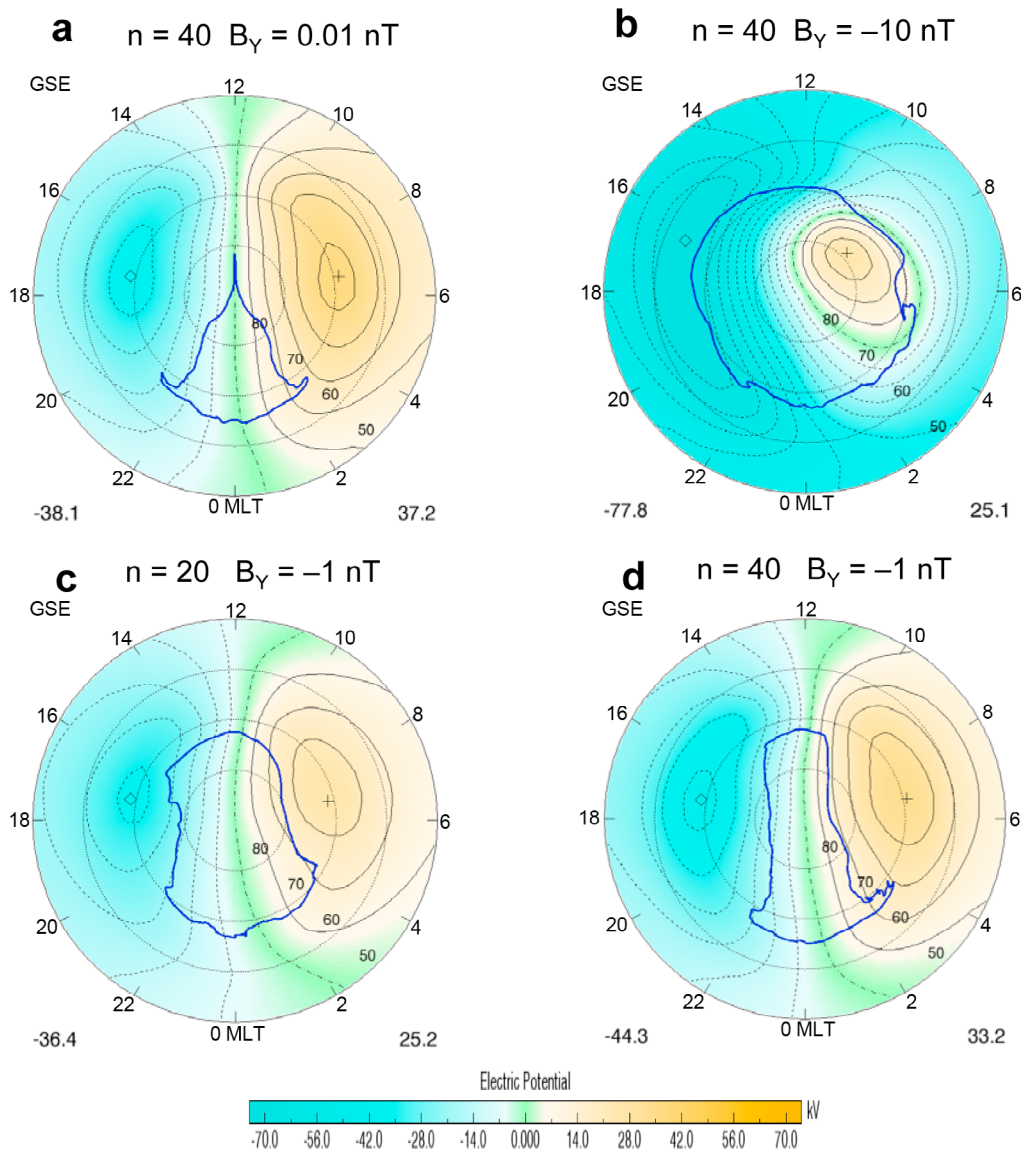
Figure 12. Ionospheric potential patterns for the northern polar cap from four ISM simulation runs. The blue contour superimposed over each pattern represents the location of the open-closed magnetic field line boundary (see section 0). The values to the left and right at the bottom of each pattern are the total potentials in the negative and positive cells, respectively.

competed during the low-|B| and high-β interval, we conducted four separate runs of the Integrated Space Model (ISM) MHD code [*White et al.*, 2001]. In all the runs B_X was set to zero to simulate conditions prevailing in the interval between lines 2 and 4. A simple way to see the differences between the runs is to examine consequent potential patterns in the high-latitude ionosphere and locations of open-closed magnetic field line boundaries. Wherever an equipotential contour crosses an open-closed boundary, merging or reconnection must have occurred to account for the change in magnetic topology. Some equipotential contours remained equatorward of the open-closed boundary. We interpret the antisunward convection portions of these contours as resulting from momentum transfer to the magnetosphere via the LLBL. Figure 12 shows four simulated

equipotential (convection) patterns in the Northern Hemisphere. Figure 12a for $n = 40$ cm^{-3} and $B_Y = -0.01$ nT (to simulate hydrodynamic coupling); Figure 12b for $n = 40$ cm^{-3} and $B_Y = -10.0$ nT (to simulate merging dominated coupling); and two intermediate cases, Figure 12c for $n = 20$ cm^{-3} and $B_Y = -1$ nT, and Figure 12d for $n = 40$ cm^{-3} and $B_Y = -1$ nT (to show mixtures of merging and hydrodynamic coupling). Plasma density and magnetic field values are like those entering the forward boundary of the simulation domain ($X_{GSE} = 40$ R_E) in the solar wind. Inputs for all runs were held constant for 2 hours to achieve stable solutions. To simplify calculations, the ionosphere was approximated as a slab at 600 km with an equivalent conductance of 6 mhos. The solar wind velocity was held constant at 400 km s^{-1}.
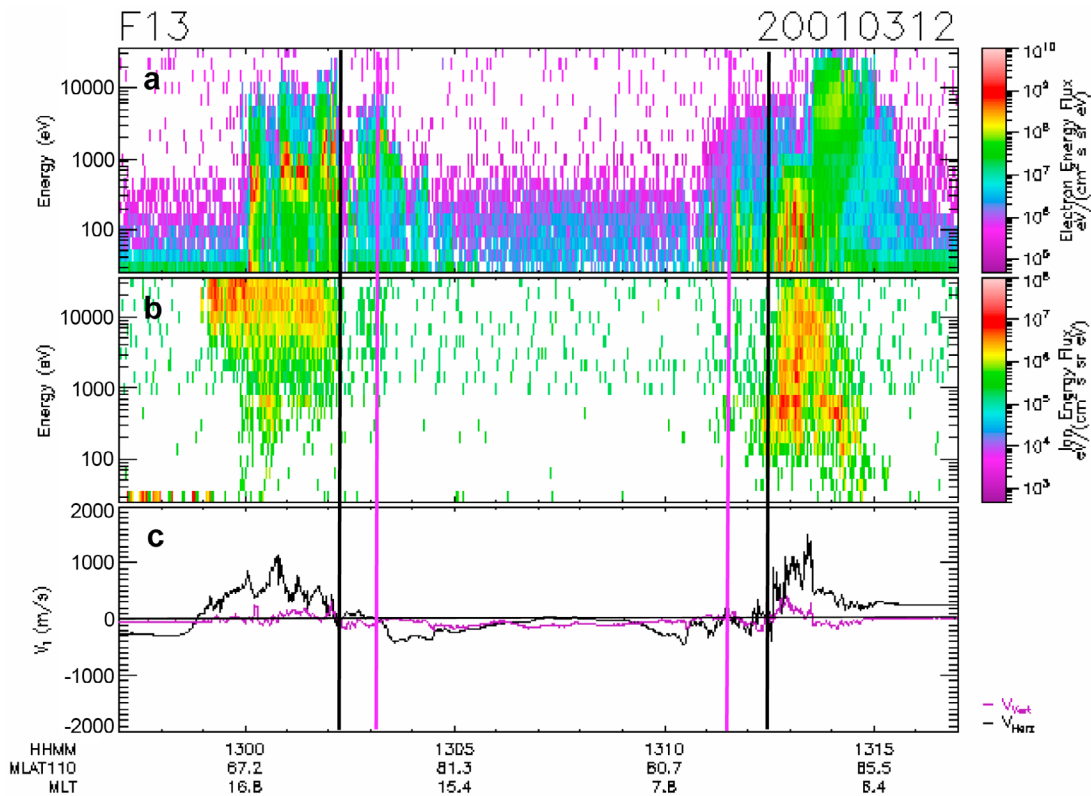
Figure 13. (a–b) Spectrograms of downward electron and ion directional differential fluxes measured during a dusk-to-dawn northern high-latitude pass of DMSP F13 just after 1300 UT. (c) Black and purple traces respectively show the simultaneously measured horizontal (V_{horiz}) and vertical (V_{vert}) components of ionospheric plasma drifts. Positive V_{horiz} indicates regions of sunward convection. Black vertical lines mark the high-latitude terminations of auroral ion fluxes. At latitudes poleward of the purple vertical lines all convection was antisunward.

[56] Conditions represented in Figure 12a may be compared with extensive simulations of the ground-state magnetosphere with "zero" IMF and a density of 5 cm^{-3} reported by *Sonnerup et al.* [2001]. They found that closed field lines on the flanks of the magnetosphere stretched beyond $X_{GSE} = -100$ R_E, consistent with an effective "viscous interaction or mass diffusion" into the LLBL. Note that in the simulation of Figure 12a all equipotentials remain on closed magnetic flux, except for a small region well poleward of the terminator which maps to the magnetotail, consistent with LLBL driving of the convection pattern. The simulated density increase from 5 cm^{-3} (in the work by *Sonnerup et al.* [2001]) to 40 cm^{-3} raised the cross-polar-cap potential from 33 to 75 kV in these totally viscous-driven cases. Simulated increases of this sort suggest that density and dynamic pressure of the solar wind can drive high-latitude convection with cross-polar-cap potentials similar to those for moderate activity in merging driven cases. The dawn and dusk regions remained symmetric in both runs. Figure 12b considers a case in which $B_Y = -10$ nT where all dynamics are merging driven. All equipotential contours reach the open field line region, but their distributions on the dawn and dusk sides are highly asymmetric [e.g., *Heppner and Maynard*, 1987]. Significant driving due to merging at high latitudes, prenoon (postnoon) in the Northern (Southern) Hemisphere, is expected [*Crooker*

et al., 1979]. Note that for +10 nT, the merging line in the Northern Hemisphere would be located at postnoon local times.

[57] Figures 12c and 12d show patterns for $B_Y = -1$ nT at densities comparable to and twice those measured at the location of ACE. An IMF of 1 nT transitions to a magnetosheath field of just under 4 nT near a quasi-perpendicular shock. This is characteristic of Polar/Cluster observations in low magnetic field regions, although some measured values were less. The equipotential patterns have slightly less dawn-dusk symmetry than in Figures 12a. Contours for about 45 of the 61 kV of cross-polar-cap potential (Φ_{PC}) in Figure 12c and about 40 of the 77 kV in Figure 12d are opened on the dayside. The remainders are LLBL driven. Increasing B_Y to -2 nT (not shown) increases the asymmetry between dawn and dusk and the percentage of open potential contours. The simulations show that the interaction with the magnetosphere is a mixture of convection driven through the LLBL on closed field lines and convection that is merging driven via an open polar cap. In the actual case, the B_Y reversal should shift the merging site to the postnoon local time sector and introduce a pause in merging during the transition [see *Maynard et al.*, 2001a].

[58] Figures 13a and 13b show spectrograms of downward electron and ion directional differential fluxes mea-sured during a dusk-to-dawn northern high-latitude pass of

DMSP F13 just after 1300 UT. Black and purple traces in Figure 13c show the simultaneously measured horizontal (V_{horiz}) and vertical (V_{vert}) components of ionospheric plasma drifts, respectively. Positive V_{horiz} indicates regions of sunward convection. Dawnside and duskside convection reversals occur between the vertical black and purple lines. Black lines mark the high-latitude terminations of observed auroral ion fluxes. At latitudes poleward of the purple lines all convection was antisunward. Attention is directed to the presence of significant energetic electron fluxes near and poleward of the purple vertical lines. The persistence of energetic electron precipitation over ~3° magnetic latitude poleward of the convection reversal on both sides of the oval indicates that they resided on closed magnetic flux. Antisunward convection of closed flux is a condition that is only met in regions that map through the LLBL [e.g., *Sonnerup*, 1980; *Sonnerup et al.*, 2001]. This, along with the lack of antisunward convection in the center of the polar cap, is consistent with the dominance of hydrodynamic driven coupling during the previous half hour. The cross-polar-cap potential of 40 kV measured by DMSP exceeds the modeled value reported by *Sonnerup et al.* [2001] for zero IMF and a solar wind density of 5 cm^{-3}, but below that for the zero IMF simulation with 40 cm^{-3} reported here. The longer that the system is under the influence of the magnetic hole associated with the HPS, the closer the magnetospheric system should approach the results produced in steady state simulations.

[59] A further consequence of the HPS-HCS passage is a sudden impulse in the northward magnetic field recorded by subauroral dayside ground magnetometers [e.g., *Le et al.*, 1993; *Russell and Ginskey*, 1995], an ionospheric current response to the HPS density increase. The International Monitor for Auroral Geomagnetic Effects (IMAGE) magnetometer chain, located postnoon between 1400 and 1500 MLT in Scandinavia, saw a positive change of nearly 100 nT, peaking near 1220 UT and then decaying (not shown). Similar to results reported by *Le et al.* [1993], the prenoon responses observed by the magnetometer at Narsarsauq, Greenland, were negative.

[60] It is important to note that low IMF values, and even lower values of **B** in the magnetosheath, do not imply the cessation of activity in the magnetosphere. The coupling mechanism mix was altered during the 45 min period while the magnetic hole passed Earth. It changed from merging driven to one dominated by pressure and viscous coupling through the LLBL. In fact, the 3 hour planetary magnetic activity index, K_P, was 3+ during the period of our case study, and the index SYM-H had a slightly negative slope, indicating that the ring current was intensifying.

7. Summary

[61] On 12 March 2001 between 1200 and 1300 UT the heliospheric current sheet separating the toward and away sectors of the IMF crossed the bow shock and passed by the magnetosphere. The interaction of the planar HPS-HCS structure with the bow shock and magnetosphere generated unusual dynamics in the magnetosheath that were monitored by Polar and Cluster. Observations within the magnetic hole include (1) low magnetic field magnitudes with |**B**| less than

the expected shocked IMF values and for short periods even less than those measured upstream by ACE; (2) values of β from 10 to 100 and above, even reaching 10,000; and (3) densities typically 80–100 cm^{-3} that exceeded 140 cm^{-3} during one interval.

[62] Comparing these observations with those detected at L_1, we conclude that the lag time from ACE to Polar and Cluster expanded from initial values less than advection times to significantly greater intervals than advection within the current sheet. The lag times returned to their original values on a time scale of ~30 min. These changes were associated with changes in IMF B_X and with the tilt of phase planes containing IMF **E** and **B** [*Maynard et al.*, 2001b; *Weimer et al.*, 2002]. The resulting expansion (and later compression) of **B** contributed to the low values of |**B**| between reference lines 2 and 4. A smaller-scale structure involving a large increase in density and |**B**| and subsequent decrease, which occurred at a reversal of B_Y, was interpreted as a magnetosonic fast wave.

[63] Values of |**B**| were extremely variable in the expanded magnetic hole. Considering analogous measurements by *Parks et al.* [2007] in the magnetotail, we suggest that the observed intense fine structure was due to nonlinear enhancement of local waves. Within the region of large-amplitude structures and low **B**, the ions became demagnetized and were thus subject to a mix of hydrodynamic and magnetohydrodynamic forcing.

[64] Through ISM simulations we showed that hydrodynamic forcing couples magnetosheath plasma to the magnetosphere through the LLBL, which is characterized by closed magnetic topology and antisunward convecting plasma. In this case of very low |**B**| and high β in the magnetosheath, a mixture of weak merging and LLBL driving is responsible for convection in the high-latitude ionosphere. A near-simultaneous DMSP F13 pass across the simulated region confirmed this conjecture through its observations of energetic electron fluxes on antisunward moving field lines on both the dawn and dusk sides of the polar cap.

[65] HPS-HCS crossings are regular occurrences whose interactions with the magnetosphere-magnetosheath system are uniquely specified by mixed hydrodynamic and magnetohydrodynamic forcing. Despite the very low magnetic fields in the associated magnetic hole, the magnetosphere-ionosphere was not devoid of magnetic activity. Understanding response to HPS-HCS crossings with its associated changing IMF B_X is important for correctly predicting the timing and dynamics of space weather events.

References

Axford, W. I., and C. O. Hines (1961), A unifying theory of high latitude geophysical phenomena and geomagnetic storms, *Can. J. Phys.*, *39*, 1433–1464.

Balogh, A., et al. (2001), The Cluster magnetic field investigation: Overview of inflight performance and initial results, *Ann. Geophys.*, *19*, 1207–1217.

Crooker, N. U. (1979), Dayside merging and cusp geometry, *J. Geophys. Res.*, *84*, 951–959.

Crooker, N. U., G. L. Siscoe, S. Shodham, D. F. Webb, J. T. Gosling, and E. J. Smith (1993), Multiple heliospheric current sheets and coronal streamer belt dynamics, *J. Geophys. Res.*, *98*, 9371–9381.

Crooker, N. U., M. E. Burton, G. L. Siscoe, S. W. Kahler, J. T. Gosling, and E. J. Smith (1996), Solar wind streamer belt structure, *J. Geophys. Res.*, *101*, 24,331–24,341.

Dungey, J. W. (1961), Interplanetary magnetic fields and the auroral zone, *Phys. Rev. Lett.*, *6*, 47–48.

Gustafsson, G., et al. (1997), The electric field and wave experiment for the Cluster mission, *Space Sci. Rev.*, *79*, 137–156, doi:10.1023/A:1004975108657.

Hain, K. (1987), The partial donor cell method, *J. Comp. Physics*, *73*, 131–147, doi:10.1016/0021-9991(87)90110-0.

Hardy, D. A., L. K. Schmidt, M. S. Gussenhoven, F. J. Marshall, H. C. Yeh, T. L. Shumaker, A. Huber, and J. Pantazis (1984), Precipitating electron and ion detectors (SSJ/4) for block 5D/flights 6–10 DMSP satellites: Calibration and data presentation, *Tech. Rep., AFGL-TR-84-0317*, Air Force Geophys. Lab., Hanscom Air Force Base, Mass.

Harvey, P., et al. (1995), The electric field instrument on the Polar satellite, *Space Sci. Rev.*, *71*, 583–596.

Heppner, J. P., and N. C. Maynard (1987), Empirical high latitude electric field models, *J. Geophys. Res.*, *92*, 4467–4489, doi:10.1029/JA092iA05p04467.

Hundhausen, A. H. (1977), An interplanetary view of coronal holes, in *Coronal Holes and High Speed Wind Streams*, edited by J. B. Zirker, pp. 225–329, Colo. Assoc. Univ. Press, Boulder, Colo.

Kahler, S., and R. P. Lin (1994), The determination of interplanetary magnetic field polarities around sector boundaries using E >2 keV electrons, *Geophys. Res. Lett.*, *21*, 1575–1578, doi:10.1029/94GL01362.

Kivelson, M. G., and C. T. Russell (Eds.) (1995), *Introduction to Space Physics*, 119 pp., Cambridge Univ. Press, New York.

Klein, L., and L. F. Burlaga (1980), Interplanetary sector boundaries 1971–1973, *J. Geophys. Res.*, *85*, 2269–2276, doi:10.1029/JA085iA05p02269.

Le, G., C. T. Russell, S. M. Petrinec, and M. Ginsky (1993), Effect of sudden solar wind dynamic pressure changes at subauroral latitudes: Change in magnetic field, *J. Geophys. Res.*, *98*, 3983–3990, doi:10.1029/92JA02397.

Lepping, R. P., et al. (1995), The Wind magnetic field investigation, *Space Sci. Rev.*, *71*, 207–229.

Lin, R. P., et al. (1995), A three-dimensional plasma and energetic particle investigation for the Wind spacecraft, *Space Sci. Rev.*, *71*, 125–153.

Lotko, W., B. Sonnerup, and R. Lysak (1987), Nonsteady boundary layer flow including ionospheric drag and parallel electric fields, *J. Geophys. Res.*, *92*, 8635–8648.

MacMahon, A. (1965), Finite gyro-radius corrections to the hydromagnetic equations for a Vlasov plasma, *Phys. Fluids*, *8*, 1840–1845, doi:10.1063/1.1761116.

Maynard, N. C., G. L. Siscoe, B. U. Ö. Sonnerup, W. W. White, K. D. Siebert, D. R. Weimer, G. M. Erickson, J. A. Schoendorf, D. M. Ober, and G. R. Wilson (2001a), Response of ionospheric convection to changes in the IMF: Lessons from a MHD simulation, *J. Geophys. Res.*, *106*, 21,429–21,451, doi:10.1029/2000JA000454.

Maynard, N. C., W. J. Burke, P. E. Sandholt, J. Moen, D. M. Ober, M. Lester, D. R. Weimer, and A. Egeland (2001b), Observations of simultaneous effects of merging in both hemispheres, *J. Geophys. Res.*, *106*, 24,551–24,577, doi:10.1029/2000JA000315.

Maynard, N. C., et al. (2003), Polar, Cluster and SuperDARN evidence for high latitude merging during southward IMF: Temporal/spatial evolution, *Ann. Geophys.*, *21*, 2233–2258.

Maynard, N. C., et al. (2006), Characteristics of merging at the magnetopause inferred from dayside 557.7 nm all-sky images: IMF drivers of poleward moving auroral forms, *Ann. Geophys.*, *24*, 3071–3098, doi:10.5194/angeo-24-3071-2006.

Maynard, N. C., W. J. Burke, D. M. Ober, C. J. Farrugia, H. Kucharek, M. Lester, F. S. Mozer, C. T. Russell, and K. D. Siebert (2007), Interaction of the bow shock with a tangential discontinuity and solar wind density decrease: Observations of predicted fast mode waves and magnetosheath merging, *J. Geophys. Res.*, *112*, A12219, doi:10.1029/2007JA012293.

Maynard, N. C., C. J. Farrugia, D. M. Ober, W. J. Burke, M. Dunlop, F. S. Mozer, H. Rème, P. Décréau, and K. D. Siebert (2008), Cluster observations of fast waves in the magnetosheath launched as a tangential discontinuity with a pressure increase crossed the bow shock, *J. Geophys. Res.*, *113*, A10212, doi:10.1029/2008JA013121.

McComas, D. J., S. J. Bame, P. Barker, W. C. Feldman, J. L. Phillips, P. Riley, and J. W. Griffee (1998), Solar wind electron proton alpha monitor (SWEPAM) for the Advanced Composition Explorer, *Space Sci. Rev.*, *86*(1-4), 563–612.

Ness, N. F., and J. M. Wilcox (1964), Solar origin of the interplanetary magnetic field, *Phys. Rev. Lett.*, *13*, 461–464.

Northrup, T. G. (1964), *The Adiabatic Motion of Charged Particles*, pp. 3–10, John Wiley, New York.

Ogilvie, K. W., et al. (1995), SWE, a comprehensive plasma instrument for the Wind spacecraft, *Space Sci. Rev.*, *71*, 55–77.

Parks, G. K., et al. (2007), Solitary electromagnetic pulses detected with super-Alfvénic flows in Earth's geomagnetic tail, *Phys. Rev. Lett.*, *98*, 265001, doi:10.1103/PhysRevLett.98.265001.

Pneuman, G. W., and R. A. Kopp (1971), Gas-magnetic field interactions in the solar corona, *Solar Phys.*, *18*, 258–270, doi:10.1007/BF00145940.

Rème, H., et al. (2001), First multispacecraft ion measurements in and near the Earth's magnetosphere with the identical Cluster Ion Spectrometry (CIS) experiment, *Ann. Geophys.*, *19*, 1303–1354.

Rich, F. J., and M. Hairston (1994), Large-scale convection patterns observed by DMSP, *J. Geophys. Res.*, *99*, 3827–3844, doi:10.1029/93JA03296.

Russell, C. T., and M. Ginskey (1995), Sudden impulses at subauroral latitudes: Response for northward interplanetary magnetic field, *J. Geophys. Res.*, *100*, 23,695–23,702, doi:10.1029/95JA02495.

Russell, C. T., J. T. Gosling, R. D. Zwickl, and E. J. Smith (1983), Multiple spacecraft observations of interplanetary shocks: ISEE three-dimensional plasma measurements, *J. Geophys. Res.*, *88*(A12), 9941–9947.

Russell, C. T., R. C. Snare, J. D. Means, D. Pierce, D. Dearborn, M. Larson, G. Barr, and G. Le (1995), The GGS/Polar magnetic field investigation, *Space Sci. Rev.*, *71*, 563–582, doi:10.1007/BF00751341.

Schulz, M. (1973), Interplanetary sector structure and the heliomagnetic equator, *Astrophys. Space Sci.*, *24*, 371–383, doi:10.1007/BF02637162.

Scudder, J. D., et al. (1995), Hydra: A three dimensional electron and ion instrument for the Polar spacecraft of the GGS mission, *Space Sci. Rev.*, *71*, 459–495.

Scudder, J. D., R. D. Holdaway, R. Glassberg, and S. L. Rodriguez (2008), Electron diffusion region and thermal demagnetization, *J. Geophys. Res.*, *113*, A10208, doi:10.1029/2008JA013361.

Smith, E. J., B. T. Tsurutani, and R. L. Rosenberg (1978), Observations of the interplanetary sector structure up to heliographic latitudes of 16°: Pioneer 11, *J. Geophys. Res.*, *83*, 717–724, doi:10.1029/JA083iA02p00717.

Sonnerup, B. U. Ö. (1980), Theory of the low latitude boundary layer, *J. Geophys. Res.*, *85*, 2017–2026, doi:10.1029/JA085iA05p02017.

Sonnerup, B. U. Ö., K. D. Siebert, W. W. White, D. R. Weimer, N. C. Maynard, J. A. Schoendorf, G. R. Wilson, G. L. Siscoe, and G. M. Erickson (2001), Simulations of the magnetosphere for zero interplanetary magnetic field: The ground state, *J. Geophys. Res.*, *106*, 29,419–29,434, doi:10.1029/2001JA000124.

Spreiter, J. R., A. L. Summers, and A. Y. Alksne (1966), Hydromagnetic flow around the magnetosphere, *Planet. Space Sci.*, *14*, 223–253.

Vasyliunas, V. M. (1975), Theoretical models of magnetic field line merging, 1, *Rev. Geophys.*, *13*, 303–336.

Weimer, D. R., D. Ober, N. C. Maynard, W. J. Burke, M. R. Collier, D. J. McComas, N. F. Ness, and C. W. Smith (2002), Variable time delays in the propagation of the interplanetary magnetic field, *J. Geophys. Res.*, *107*(A8), 1210, doi:10.1029/2001JA009102.

White, W. W., J. A. Schoendorf, K. D. Siebert, N. C. Maynard, D. R. Weimer, G. L. Wilson, B. U. Ö. Sonnerup, G. L. Siscoe, and G. M. Erickson (2001), MHD simulation of magnetospheric transport at the mesoscale, in *Space Weather*, *Geophys. Monogr. Ser.* vol. 125, edited by P. Song, H. J. Singer, and G. L. Siscoe, pp. 229–240, AGU, Washington, D. C.

Wilcox, J. M., and N. F. Ness (1965), Quasi-stationary corotating structure in the interplanetary medium, *J. Geophys. Res.*, *70*, 5793–5805, doi:10.1029/JZ070i023p05793.

Winterhalter, D., E. J. Smith, M. E. Burton, N. Murphy, and D. J. McComas (1994), The heliospheric plasma sheet, *J. Geophys. Res.*, *99*, 6667–6680, doi:10.1029/93JA03481.

W. J. Burke and D. M. Ober, Air Force Research Laboratory, Hanscom Air Force Base, 29 Randolph Rd., Bedford, MA 01731-3010, USA.

C. J. Farrugia, N. C. Maynard, and C. Mouikis, Space Science Center, University of New Hampshire, Durham, NH 03842, USA. (nelson.maynard@unh.edu)

F. S. Mozer, Space Sciences Laboratory, University of California, Berkeley, CA 94720, USA.

H. Rème, Centre d'Etude Spatiale des Rayonnements, CNRS, Avenue du Colonel Roche, 31028 Toulouse Cédex 4, France.

C. T. Russell, Institute of Geophysics and Planetary Physics, University of California, 603 Charles E. Young Dr. E., Los Angeles, CA 90065-1567, USA.

J. D. Scudder, Department of Physics and Astronomy, University of Iowa, 203 Van Allen Hall, Iowa City, IA 52242-1479, USA.

K. D. Siebert, Applied Research Associates, Inc., Nashua, NH 03060, USA.